

# Observational Properties of Simulated Galaxies in Overdense and Average Regions at Redshifts $z \simeq 6 - 12$

Hidenobu Yajima<sup>1,2,3\*</sup>, Isaac Shlosman<sup>3,4</sup>, Emilio Romano-Díaz<sup>5</sup>, Kentaro Nagamine<sup>3,6</sup>

<sup>1</sup> Frontier Research Institute for Interdisciplinary Sciences, Tohoku University, Sendai 980-8578, Japan

<sup>2</sup> Astronomical Institute, Tohoku University, Sendai 980-8578, Japan

<sup>3</sup> Department of Earth & Space Science, Graduate School of Science, Osaka University, 1-1 Machikaneyama, Toyonaka, Osaka 560-0043, Japan

<sup>4</sup> Department of Physics & Astronomy, University of Kentucky, Lexington, KY 40506-0055, USA

<sup>5</sup> Argelander Institut fuer Astronomie, University of Bonn, Auf dem Haegel, 71, D-53121 Bonn, Germany

<sup>6</sup> Department of Physics & Astronomy, University of Nevada, Las Vegas, 4505 S. Maryland Pkwy, Las Vegas, NV 89154-4002, USA

Accepted ??; Received ??; in original form ???

## ABSTRACT

We use high-resolution zoom-in cosmological simulations of galaxies of Romano-Díaz et al., post-processing them with a panchromatic three-dimensional radiation transfer code to obtain the galaxy UV luminosity function (LF) at  $z \simeq 6 - 12$ . The galaxies are followed in a rare, heavily overdense region within a  $\sim 5\sigma$  density peak, which can host high- $z$  quasars, and in an average density region, down to the stellar mass of  $M_{\text{star}} \sim 4 \times 10^7 M_{\odot}$ . We find that the overdense regions evolve at a substantially accelerated pace — the most massive galaxy has grown to  $M_{\text{star}} \sim 8.4 \times 10^{10} M_{\odot}$  by  $z = 6.3$ , contains dust of  $M_{\text{dust}} \sim 4.1 \times 10^8 M_{\odot}$ , and is associated with a very high star formation rate,  $\text{SFR} \sim 745 M_{\odot} \text{ yr}^{-1}$ . The attained  $\text{SFR} - M_{\text{star}}$  correlation results in the *specific* SFR slowly increasing with  $M_{\text{star}}$ . Most of the UV radiation in massive galaxies is absorbed by the dust, its escape fraction  $f_{\text{esc}}$  is low, increasing slowly with time. Galaxies in the average region have less dust, and agree with the observed UV LF. The LF of the overdense region is substantially higher, and contains much brighter galaxies. The massive galaxies are bright in the infrared (IR) due to the dust thermal emission, with  $L_{\text{IR}} \sim 3.7 \times 10^{12} L_{\odot}$  at  $z = 6.3$ , while  $L_{\text{IR}} < 10^{11} L_{\odot}$  for the low-mass galaxies. Therefore, ALMA can probe massive galaxies in the overdense region up to  $z \sim 10$  with a reasonable integration time. The UV spectral properties of disk galaxies depend significantly upon the viewing angle. The stellar and dust masses of the most massive galaxy in the overdense region are comparable to those of the sub-millimetre galaxy (SMG) found by Riechers et al. at  $z = 6.3$ , while the modelled SFR and the sub-millimetre flux fall slightly below the observed one. Statistical significance of these similarities and differences will only become clear with the upcoming ALMA observations.

**Key words:** radiative transfer – galaxies: formation – infrared: galaxies – ultraviolet: galaxies – methods: numerical – dust, extinction

## 1 INTRODUCTION

Understanding galaxy evolution in the high-redshift universe is one of the major goals in contemporary astronomy. To reveal the mechanism(s) of this evolution, it is crucial to study the galactic spectra reflecting their physical state, e.g., star formation rate (SFR), stellar mass, metallicity, dust contents, and their spatial distributions. In this work, we investigate the UV spectral properties (including the UV luminosity function) of high- $z$  galaxies in a rare overdense region

of the universe in the wide redshift range of  $z \simeq 6 - 12$ , and compare them with an average density region. We calculate the UV continuum, both intrinsic and attenuated by dust, estimate the FIR emission from the dust, and analyze their observational corollaries.

At high redshifts,  $z \gtrsim 6$ , thousands of galaxies have been detected using the drop-out technique in the UV band — the so-called Lyman break galaxies (LBGs: Shapley et al. 2003; Bouwens et al. 2009, 2010, 2011, 2012, 2014b; Ouchi et al. 2009; McLure et al. 2013; Ellis et al. 2013; Oesch et al. 2012, 2013; Finkelstein et al. 2014). These LBGs are typical star-forming galaxies at high- $z$ , and have

\* E-mail: yajima@roe.ac.uk

been used to probe the cosmic star formation (SF) history (e.g., Madau et al. 1999; Madau & Dickinson 2014; Steidel et al. 1999; Ouchi et al. 2004; Hopkins & Beacom 2006; Bouwens et al. 2007, 2014b, see also the review by Shlosman 2013). Another population of high-redshift star-forming galaxies is the Lyman- $\alpha$  emitters (LAEs) which are identified by Ly $\alpha$  lines (e.g., Iye et al. 2006; Gronwall et al. 2007; Ouchi et al. 2010; Blanc et al. 2011; Vanzella et al. 2011; Ono et al. 2012; Shibuya et al. 2012; Finkelstein et al. 2013). LBGs and LAEs are thought to be young star-forming galaxies with little dust.

Large column densities of dust attenuate the UV continuum and the Ly $\alpha$  photons, and galaxies become fainter than the detection limits for current observations. Massive galaxies can possess dust produced by type II supernovae (SNe) via earlier SF<sup>1</sup> (e.g., Todini & Ferrara 2001; Schneider et al. 2004; Nozawa et al. 2007; Hirashita et al. 2014). This dust can absorb the UV photons and re-emit the energy in the infrared band as a thermal emission. Modern sub-millimetre telescopes, e.g., ALMA or the Herschel satellite, are gradually opening the window for detection of distant SMGs. A recently discovered SMG at  $z = 6.3$  (Riechers et al. 2013) exhibits  $\text{SFR} \sim 2900 M_{\odot} \text{ yr}^{-1}$  and a dust mass of  $M_{\text{dust}} \sim 10^9 M_{\odot}$ . Thus, at  $z \gtrsim 6$ , the radiation properties of galaxies show a wide range, involving SMGs, LBGs, LAEs, etc.

A number of cosmological simulations have been carried out to reproduce the typical star-forming galaxies at high- $z$  in the mean density fields (e.g., Nagamine et al. 2004; Romano-Díaz et al. 2009; Finlator et al. 2011; Yajima et al. 2012a,c,b, 2014b; Jaacks et al. 2013; Wise et al. 2012, 2014; Paardekooper et al. 2013), or massive galaxies in rare overdense regions by using large computational boxes (e.g., Di Matteo et al. 2005; Li et al. 2007; Cen & Zheng 2013) or Constrained Realizations (e.g., Romano-Díaz et al. 2011b, 2014). While the physical state of galaxies in various fields have been investigated, their spectral properties are not well known, requiring detailed radiative transfer (RT) calculations. Simulations, which attempt to infer observational properties without RT, must make additional assumptions, such as the spatial distribution of dust, etc. (e.g., Nagamine et al. 2010b; Dayal & Ferrara 2012; Shimizu et al. 2014).

As a next step, the dust extinction should be estimated by means of the RT, and the emergent radiation properties can be compared to the observations. By applying RT, the actual stellar and dust distributions will be considered, and the optical depth for relevant photons will be calculated. Dayal et al. (2013) investigated radiation properties of galaxies in cosmological simulations by using a simple dust screening model, and reproduced the statistical properties of observed LBGs at  $z \gtrsim 6$ . However, since the dust is distributed inhomogeneously in galaxies, numerical simulations are required to calculate the RT along various directions and from a large number of stars. Combining cos-

mological Smoothed Particle Hydrodynamics (SPH) simulations with the post-processed RT, Yajima et al. (2014b) analyzed the dust extinction of star-forming galaxies at  $z = 3$ , and have reproduced the observed luminosity function (LF) adopting a SN dust model. The LF was found to be moderately insensitive to dust properties, e.g., composition, grain size, and dust-to-metal mass ratio, despite that the colour in the UV bands is known to depend sensitively on the dust properties. In particular, they found that the dust composition cannot be of a purely silicate type. Instead, the graphite type should be the dominant component in order to reproduce the observed extinction level and the rest-frame UV LF of LBGs at this redshift.

Using cosmological adaptive mesh refinement (AMR) simulations and RT calculations, Kimm & Cen (2013) have recently analyzed the dust extinction of the UV stellar radiation in galaxies at  $z = 7$  with stellar masses of  $5 \times 10^8 M_{\odot} - 2.5 \times 10^{10} M_{\odot}$ , and have shown that most of the UV radiation is absorbed by dust. In a companion paper, Cen & Kimm (2014) have further investigated the infrared properties of these model galaxies. These calculations have followed a density peak in a box of  $120 h^{-3} \text{Mpc}^3$ , corresponding to a  $1.8\sigma$  fluctuation, which led to a peak  $\text{SFR} \sim 100 M_{\odot} \text{ yr}^{-1}$  at  $z \sim 7$ , and formation of a galaxy cluster of  $\sim 3 \times 10^{14} M_{\odot}$  by  $z \sim 0$ . The sample was limited to  $z = 7$  and to 198 massive galaxies in the biased region — the observational properties of galaxies did not include the rare overdense regions analysed here which can serve as an environment for the high- $z$  quasars.

Here we investigate the UV and IR observational properties of high- $z$  galaxies in rare overdense and average regions, using the cosmological simulations of Romano-Díaz et al. (2014) (see also Romano-Díaz et al. 2011b). They have shown that massive galaxies tend to have extended gas disks due to the efficient gas accretion from the intergalactic medium (IGM) (see also Pawlik et al. 2011). The presence of extended disks in these galaxies appear robust against the strong radiative feedback (Pawlik et al. 2013). Hence, we anticipate that when the gaseous/stellar disks form, their spectral properties change significantly, depending on the viewing angles, i.e., the “orientation effect” (Yajima et al. 2012c; Verhamme et al. 2012). These works have analyzed the orientation effect for low-mass star-forming galaxies  $M_h \sim 10^{11} M_{\odot}$  like LAEs. For the first time, we turn our attention to the orientation effects in the UV properties of high- $z$  massive galaxies in a cosmological context.

Our paper is organized as follows. We describe the simulations and our method for the radiative transfer calculations in Section 2. In Section 3, we present our results, show the simulated UV fluxes, escape fraction of non-ionizing photons, the infrared dust emission with detectability by ALMA, as well as investigate the effect of the disk galaxy orientation on the UV properties. In Section 4, we discuss our results and summarize our main conclusions.

## 2 NUMERICAL MODELLING

### 2.1 Hydrodynamic Simulations

We use the high-resolution numerical simulations of Romano-Díaz et al. (2011b, 2014), which were performed

<sup>1</sup> Note that the dominant channel for dust formation is being debated. For example, dust can also be grown in molecular clouds and produced in stellar winds from the AGB stars (e.g., Draine 2003). Since we focus on the early universe in this work, we assume that the dust is produced mainly by the SNe.

with the modified tree-particle-mesh SPH code GADGET-3 (originally described in Springel 2005) in its conservative entropy formulation (Springel & Hernquist 2002). The simulations were evolved from  $z = 199$  to  $z \sim 6$ . They include radiative cooling by H, He and metals (e.g., Choi & Nagamine 2009), star formation, stellar feedback, a galactic wind model, and a sub-resolution model for multiphase interstellar medium (ISM; Springel & Hernquist 2003a). In this model, starforming gas particles contain both the cold phase (which contributes to the gas mass and forms stars) and the hot phase (that results from the SN heating and determines the gas pressure).

The SF prescription is based on the *Pressure* model (Schaye & Dalla Vecchia 2008; Choi & Nagamine 2010) which reduces the high- $z$  SFR relative to the prescription by Springel & Hernquist (2003b). The *Pressure* model uses the conversion between the gas Jeans column density,  $\Sigma_{\text{gas},J}$ , and its mass density, i.e.,  $\Sigma_{\text{gas},J} \sim \rho_{\text{gas}} L_J = \sqrt{(\gamma/G)} f_g P_{\text{tot}}$  (Schaye & Dalla Vecchia 2008; Choi & Nagamine 2010), where  $L_J$  is the Jeans length,  $f_g$  is the gas mass fraction,  $P_{\text{tot}}$  its total pressure, i.e., thermal, turbulent, etc., and  $\gamma = 5/3$ . If the gas column density  $\Sigma_{\text{gas}}$  exceeds  $\sim 10 M_{\odot} \text{pc}^{-2}$ , the stars form with the rate  $\Sigma_{\text{SFR}} = 2.5(\Sigma_{\text{gas}}/10 M_{\odot} \text{pc}^{-2})^{1.4} M_{\odot} \text{yr}^{-1} \text{kpc}^{-2}$  (Kennicutt 1998a,b). Within this model, the SF only takes place when the gas density rises above the threshold,  $n_{\text{H,SF}} = 0.6 \text{cm}^{-3}$ . The zoom-in technique was employed in the simulations, with the gas being present only in the high-resolution region. Since the UV background intensity is not strong until the end of the cosmic reionization epoch (e.g., Faucher-Giguère et al. 2009), we do not consider it. Note that, however, the UV background can locally be strong at near star-forming galaxies and has impact on galaxy evolution (e.g., Wise et al. 2012, 2014).

Low-mass galaxies are expected to be sensitive to stellar feedback, especially in the early universe, because of their shallow potential well, making it easier for the gas to be pushed out. In an associated work, we analyze various prescriptions for feedback and compare the results with observations (Sadoun et al. in preparation). Current runs are based on the Springel & Hernquist (2003a) phenomenological wind model. This wind is driven by the SNe heating of the hot phase in the ISM whose cooling timescale is long. The cold phase of the ISM is heated and evaporated via thermal conduction from the hot phase. The mass-transfer equations between the phases are solved, based on the equilibrium model of Springel & Hernquist (2003a). The ‘wind’ SPH particles are temporarily not subject to hydrodynamical forces. The timescale for turning off the hydrodynamic interactions for the wind particle is either 50 Myr or when the background gas density has fallen by a factor of 10, whichever happens first.

## 2.2 Simulation Setup and Initial Conditions

Romano-Díaz et al. (2011b, 2014) have used two types of initial conditions (ICs). First, they followed up the high-redshift galaxy evolution in the mean density region in the universe, their so-called unconstrained (UCR) run. Second, they have applied the Constrained Realization (CR) method (e.g., Hoffman & Ribak 1991; van de Weygaert & Bertschinger 1996; Romano-Díaz et al.

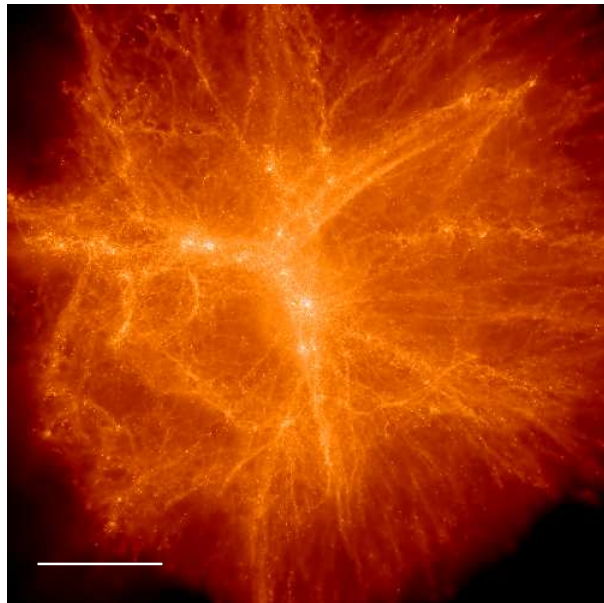


**Figure 1.** Projected gas density of the CR run at  $z = 6.3$ . The white bar represents  $1 h^{-1} \text{Mpc}$  in comoving coordinates.

2011a) to the UCR initial conditions to simulate the rare overdense region of  $\sim 5\sigma$ . These ICs have been constrained to include a seed of a massive halo of  $\sim 10^{12} h^{-1} M_{\odot}$ , projected to collapse by  $z \sim 6$  according to the top-hat model, hereafter the CR run.

A CR of a Gaussian field is defined as a random realization of such field, and is constructed to obey a set of imposed linear constraints on this field, using the method of Hoffman & Ribak (1991) and Romano-Díaz et al. (2011a, see Appendix for a comprehensive explanation of the method), by providing the optimal algorithm to create the CRs, which have been used for setting the specific ICs applied here. The large-scale properties in both ICs are the same.

The ICs have been imposed onto a grid of 1024 (CR) and 512 (UCR) cells per dimension in a cubic box of  $20 h^{-1} \text{Mpc}$ . The  $\Lambda\text{CDM}$ -WMAP5 cosmology has been adopted with  $\Omega_{\text{m}} = 0.28$ ,  $\Omega_{\Lambda} = 0.72$ , and  $\Omega_{\text{b}} = 0.045$  (Dunkley et al. 2009). Here,  $h = 0.701$  is the Hubble constant in units of  $100 \text{km s}^{-1} \text{Mpc}^{-1}$ . The power spectrum has been normalized by the linear rms amplitude of mass fluctuations in  $8 h^{-1} \text{Mpc}$  spheres extrapolated to  $z = 0$ ,  $\sigma_8 = 0.817$ . The vacuum boundary conditions have been used, and the simulations have been performed in comoving coordinates.

The gas is present only in the high-resolution regions of radius  $3.5 h^{-1} \text{Mpc}$  for the CR run, and  $7 h^{-1} \text{Mpc}$  for the UCR run. The UCR volume is matched to contain the same amount of total matter as the CR run. The general parameters of the simulations are summarized in Table 1. The spatial resolution ranges from physical  $23 h^{-1} \text{pc}$  at  $z = 12$  to  $43 h^{-1} \text{pc}$  at  $z = 6$ . Galaxies are identified with the HOP group-finder algorithm (Eisenstein & Hut 1998) for densities exceeding  $0.01 n_{\text{H,SF}}$  following Romano-Díaz et al. (2014).

To study the spectral properties of simulated galaxies at  $z = 6.3, 7, 8, 9, 10, 11$  and  $12$ , we selected galaxies with

Parameters of Cosmological Simulations

	$N_{\text{SPH}}$	$R_{\text{box}}$ ( $h^{-1}\text{Mpc}$ )	$R_{\text{box}}^{\text{zoom}}$ ( $h^{-1}\text{Mpc}$ )	$m_{\text{DM}}$ ( $h^{-1}M_{\odot}$ )	$m_{\text{SPH}}$ ( $h^{-1}M_{\odot}$ )	$m_{\text{star}}$ ( $h^{-1}M_{\odot}$ )	$\epsilon$ (pc, comoving)
CR	$1024^3$	20	3.5	$4.66 \times 10^5$	$1.11 \times 10^5$	$5.55 \times 10^4$	300
UCR	$512^3$	20	7.0	$3.73 \times 10^6$	$8.90 \times 10^5$	$4.40 \times 10^5$	300

**Table 1.**  $N_{\text{SPH}}$  is an effective number of the SPH particles in the zoom-in regions.  $R_{\text{box}}$  and  $R_{\text{box}}^{\text{zoom}}$  are radii of the entire computational box and the zoom-in regions.  $m_{\text{DM}}$ ,  $m_{\text{SPH}}$  and  $m_{\text{star}}$  are the masses of DM, gas and stellar particles.  $\epsilon$  is the gravitational softening length (comoving).

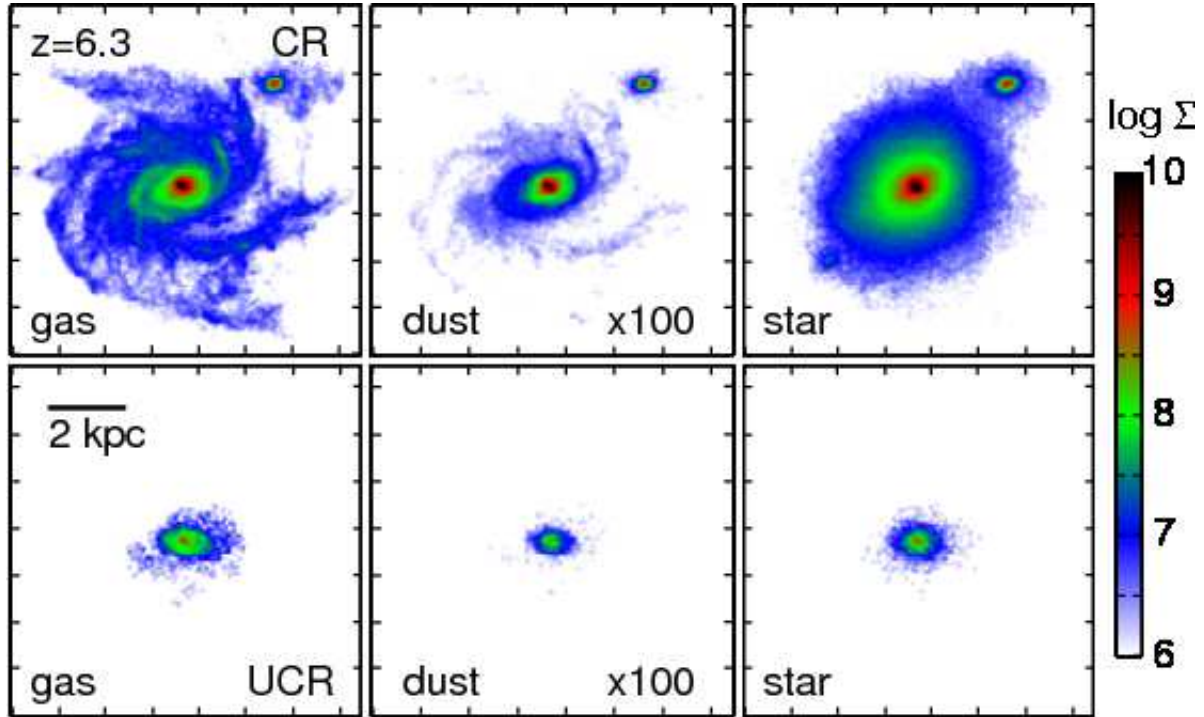


**Figure 2.** Projected gas, dust and stellar densities at  $z = 6.3$ . The colour palette represents the mass density in units of  $M_{\odot} \text{kpc}^{-2}$  on the log scale. The upper row represents the most massive galaxy in the CR run ( $M_{\text{star}} \sim 8.4 \times 10^{10} M_{\odot}$  and  $M_{\text{gas}} \sim 4.8 \times 10^{10} M_{\odot}$ ). The lower row shows the most massive galaxy in the UCR run,  $M_{\text{star}} \sim 1.5 \times 10^9 M_{\odot}$  and  $M_{\text{gas}} \sim 3.1 \times 10^9 M_{\odot}$ . The dust densities have been artificially boosted by factor of 100 for easy comparison with others in this figure. Each panel size is 9 kpc in physical units.

$M_{\text{star}} \gtrsim 4 \times 10^7 M_{\odot}$ , which corresponds to  $\gtrsim 720$  and  $\gtrsim 90$  stellar particles for CR and UCR runs, respectively. Our samples consist of 2273 and 1789 galaxies for the CR and UCR run, respectively, totaling 4062 galaxies.

Figure 1 shows a rendering of the projected gas density of the central zoomed-in region in the CR run at  $z = 6.3$ . The yardstick represents the scale of  $1 h^{-1} \text{Mpc}$ . Note the filamentary structure and the brightest regions representing galaxies. The most massive galaxy, which is a disk galaxy, is located near the centre of the zoomed-in region, and grows predominantly via the cold gas accretion from the cosmic filaments, supplemented by minor mergers (Romano-Díaz et al. 2014).

### 2.3 Radiation Transfer Calculations

For the post-processing, we carry out the RT calculations using the Monte Carlo method in the ‘All-wavelength Radiation Transfer with Adaptive Refinement Tree’ (ART<sup>2</sup>)

code to study the multi-wavelength properties of the model galaxies. The detailed prescriptions of the code have been presented in Li et al. (2008) and Yajima et al. (2012a). We solve the RT of  $10^6$  photon packets for each galaxy, which have shown good convergence in the emergent luminosity and  $f_{\text{esc}}$  (Yajima et al. 2012a). In this work, we focus on the stellar continuum radiation at  $\lambda > 912 \text{ \AA}$ , in the rest frame. Photons at UV-to-optical band can be absorbed by the interstellar dust, then re-emitted as a thermal emission in the IR. The dust temperature and its thermal emission have been estimated assuming a radiative equilibrium (Li et al. 2008). Our simulations follow the interactions between the photons and the dust on the adaptive refinement grids constructed by using positions of the SPH particles. The spatial resolution of the grids corresponds to that of the original hydrodynamics simulations. At high redshifts ( $z \gtrsim 6$ ) the dust is mainly produced by type-II SNe (e.g., Hirashita et al. 2014). The SN dust model by Todini & Ferrara (2001) is assumed here, and its opacity curve was shown in Li et al. (2008). More-

over, Yajima et al. (2014b) have shown that the observed UV radiation properties of high- $z$  galaxies are reproduced well in the cosmological simulations with the RT calculations using the SN dust model.

In the local star-forming galaxies, the dust mass is proportional to the metal mass (Draine et al. 2007). Using the metallicity of each SPH particle, we determine the dust mass of each cell under the assumption of constant dust-to-metal mass ratio,  $M_{\text{dust}}/M_{\text{metal}} = 0.4$ , i.e.,  $M_{\text{dust}} = 0.008 M_{\text{gas}} (Z/Z_{\odot})$ , where  $Z_{\odot} = 0.02$ . Based on the two-phase model of ISM in GADGET-3 (Springel 2005), we also separate the gas in each cell into the cold clumpy gas and the hot surrounding ISM. The gas phases are balanced by the thermal pressure, and the photons travel in the clumpy dusty gas (Li et al. 2008).

Current cosmological simulations still cannot resolve the propagation of the SNe shocks. In our subgrid wind model, the wind particles move with the speed of  $\sim 500 \text{ km s}^{-1}$ , and we expect that internal shocks will heat the wind to corresponding  $\sim 10^7 \text{ K}$ . At such temperatures and wind densities, the dust is destroyed by thermal sputtering process in less than the wind crossing time (e.g., Nozawa et al. 2006). Therefore, we ignore the dust in the wind altogether.

The intrinsic spectral stellar energy distributions (SEDs) have been calculated with the stellar synthesis code, Starburst99 (Leitherer et al. 1999) with a Salpeter initial mass function (Salpeter 1955). We have calculated also the radiation properties of galaxies at different viewing angles with 50 bins ( $N_{\theta} = 5$  and  $N_{\phi} = 10$ ), and analysed the orientation effects.

We have compared our CR run with a downgraded resolution of it (from  $2 \times 1024^3$  to  $2 \times 512^3$ ), both drawn from the same ICs and found no significant differences in galaxy morphologies and the distributions and fractions of the ISM (Romano-Díaz et al. 2011b, 2014; Sadoun et al. in preparation). Our spatial resolution by the end of the simulations is  $\sim 43h^{-1} \text{ pc}$  in the physical scale, which allows us to trace the clumpy ISM on scales  $\gtrsim 100 \text{ pc}$ .

### 3 RESULTS

We present our results starting with the physical properties of the galaxy population in the CR and UCR runs, then continue with the appearance of these galaxies in the UV and IR bands. We present their UV luminosity functions, redshift evolution, and the effect of galactic morphology on the spectral properties of high- $z$  galaxies.

#### 3.1 Physical properties of galaxies

The most massive galaxy in the CR run exhibits a resilient morphology of a gas-rich disk galaxy with a stellar bar and outer spiral arms, over a substantial period of time,  $z \sim 6 - 10.5$ , as shown in Figure 2 for  $z = 6.3$  and discussed in Romano-Díaz et al. (2011b). The bar is persistent, but is difficult to observe after  $z \sim 6.4$  due to an ongoing merger. This figure displays the projected gas, dust and stellar densities at  $z = 6.3$ . Located in the highly overdense region, the galaxy grows predominantly by a cold gas accretion. The galaxy experiences a SFR of  $\sim 745 M_{\odot} \text{ yr}^{-1}$

Fitting Parameters			
$X$	$Y$	$\alpha$	$\beta$
$\log M_{\text{star}}$	$\log \text{SFR}$	1.18	-10.00
$\log M_{\text{star}}$	$\log f_{\text{esc}}$	-0.34	2.15
$\log M_{\text{star}}$	$m_{\text{UV}}^{\text{int}}$	-2.69	51.00
$\log M_{\text{star}}$	$m_{\text{UV}}$	-1.88	46.13
$\log M_{\text{star}}$	$\log S_{1.1}$	0.90	-9.89
$\log M_{\text{star}}$	$\log L_{\text{IR}}$	1.12	0.42
$\log M_{\text{star}}$	$\log M_{\text{dust}}$	1.01	-3.22
$Y = \alpha X + \beta$			

**Table 2.** Fitting parameters for the relation between stellar mass and observational properties at  $z = 6.3$ . The fitting equation is  $Y = \alpha X + \beta$  with free parameters  $\alpha$  and  $\beta$ .  $m_{\text{UV}}^{\text{int}}$  and  $m_{\text{UV}}$  give the UV flux without and with dust extinction, respectively.  $S_{1.1}$  is the flux at 1.1 mm in the observer’s frame. The fitting parameters have been derived using all samples over the range of redshifts.

accumulating a  $M_{\text{star}} \sim 8.7 \times 10^{10} M_{\odot}$ . The amount of dust is  $\sim 4.1 \times 10^8 M_{\odot}$ , and the mean gas metallicity has reached  $Z \sim 0.7 Z_{\odot}$ . This dust is concentrated around the galactic center, while the stellar distribution is more extended and exhibits also a spheroidal component.

In comparison, the most massive galaxy in the UCR run is more compact and spheroidal. The half-mass radius of the gaseous (stellar) distribution in the most massive UCR galaxy at  $z \sim 6.3$  is about 375 pc (255 pc). Most of the baryons are enclosed within the central kpc, and its SFR is  $\sim 8.8 M_{\odot} \text{ yr}^{-1}$ , which is a factor of  $\sim 80$  lower than that of the most massive object in the CR run. More detailed analysis of the galactic morphology will be shown elsewhere.

The evolution of SFR, gas metallicity and dust mass as a function of the galaxy stellar mass are shown in Figure 3. For each redshift, the SFR increases nearly linearly with the stellar mass and its slope  $\alpha$  in the log-log plot ranges within  $\sim 1.00 - 1.27$ , which is consistent with the previous works (e.g., Finlator et al. 2011). The slopes for all the samples are summarized in Table 2. Such slopes imply a weak dependence of the specific SFR (sSFR) on  $M_{\text{star}}$ , where  $\text{sSFR} \equiv \text{SFR}/M_{\text{star}}$ . This trend is also supported by observations (e.g., Ono et al. 2010). As  $\alpha \gtrsim 1$ , the sSFR slightly increases with  $M_{\text{star}}$  — contrary to what has been found for lower redshifts (Stark et al. 2009, 2013). We find also that the sSFR decreases somewhat with redshift, as can be seen in the second panels (from the top) of Figure 3. This trend and values are consistent with recent simulations (Nagamine et al. 2010b; Dayal et al. 2013; Biffi & Maio 2013) and observations (Stark et al. 2013; Oesch et al. 2014). Such a trend seems to reflect dependence of the sSFR on the gas fraction in galaxies which decreases with redshift for the low-mass galaxies. Some of the lower-mass galaxies are affected more by the stellar feedback, while the higher-mass galaxies retain much of their gas, keeping their high SFRs. This causes a substantially higher dispersion in the SFR for galaxies with  $M_{\text{star}} \lesssim 10^9 M_{\odot}$ .

We do not observe any clear difference in the SFR –  $M_{\text{star}}$  relationship between the CR and UCR runs, except

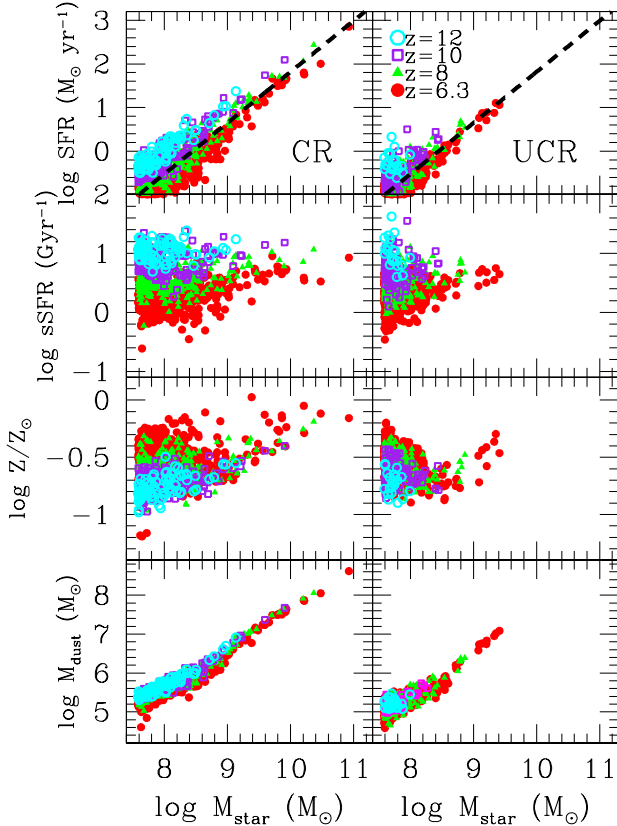


**Figure 3.** Star formation rate (SFR), specific star formation rate (sSFR), mean gas metallicity in units of the solar metallicity ( $Z/Z_{\odot}$ ), and galactic dust mass ( $M_{\text{dust}}$ ), as a function of the galaxy stellar mass ( $M_{\text{star}}$ ). The different symbols represent the different redshifts,  $z = 6.3, 8, 10$  and  $12$ .

the presence of much higher galaxy masses in the former. The SFR of most galaxies in the CR and UCR runs is fueled by the cold gas accretion rather than by major mergers, as shown by Romano-Díaz et al. (2014). Obviously, the upper cutoff of the SFR lies much lower for the UCR run because of the absence of massive galaxies in the normal region at  $z \sim 6$ . This cutoff is increasing with time, e.g., it is  $\sim 124 M_{\odot} \text{ yr}^{-1}$  at  $z \sim 10$  and  $745 M_{\odot} \text{ yr}^{-1}$  at  $z \sim 6.3$ , for the CR run.

One expects that galaxy evolution process is greatly accelerated in the overdense regions, which is supported by the evolution of the CR galaxies. The third panels (from the top) of Figure 3 show that the gas metallicity  $Z/Z_{\odot}$  has a large dispersion, because the gas in low-mass galaxies is easily blown away by the SN feedback. In these objects, the metallicity can quickly rise to  $\log(Z/Z_{\odot}) \sim -0.5$  once the stars form, and it will lead to a large dispersion, reflecting the variation in the SFRs. On the other hand, massive galaxies show a tighter correlation owing to the steady gas supply from the IGM filaments and minor mergers — the width of quartiles to median values at each mass bin decreases with increasing mass. Metallicity of some massive galaxies in the CR run reaches a nearly solar abundance at  $z \sim 6.3$ . Already at  $z \sim 10$ , the most massive galaxy exhibits  $\log(Z/Z_{\odot}) \sim -0.4$  due to early SF. There is little difference in the value and

the spread between the CR and UCR runs. Most of the difference again becomes visible for  $M_{\text{star}} \gtrsim 10^9 M_{\odot}$ . The observed LBGs at  $z \lesssim 5$  show metallicities ranging from  $\sim 0.1$  to  $\sim 0.4 Z_{\odot}$  (e.g., Pettini et al. 2001; Shapley et al. 2003; Maiolino et al. 2008; Nakajima et al. 2013). Our CR results exhibit similar median metallicities, with only a few outliers having near-solar abundances.

However, the halos of the massive galaxies in CR have already reached the mass range of  $\sim 10^{12} M_{\odot}$  by  $z \sim 6$ , which is similar to that of the observed LBGs at  $z < 5$  (e.g., Ouchi et al. 2004). Galaxies in overdense region evolve ahead of the normal regions. Therefore, these massive galaxies can be substantially enriched by metals during this rapid galaxy growth. In addition, there is little information about the metallicity of galaxies at  $z > 6$  due to difficulties in detecting the metal lines. Bouwens et al. (2010) have noted a very low metallicity of LBGs at  $z \sim 7$  from the extreme blue colors of their UV spectra, while in the recently observed large sample, the UV slope of LBGs at  $z > 6$  appears similar to that of galaxies at  $z \lesssim 5$  (Dunlop et al. 2012; Bouwens et al. 2014a). Hence, the metallicity of galaxies at  $z \gtrsim 6$  is still subject to debate.

The bottom two panels of Figure 3 show that the galactic dust mass,  $M_{\text{dust}}$ , is tightly correlated with the stellar mass, because  $\sim 0.14$  of the stellar mass ends up as type-II SNe, and the amount of dust is fixed (Todini & Ferrara 2001). On the other hand, some fraction of dust is consumed by the SF process or is blown out of galaxies by the SNe feedback. Again, this increases dispersion in  $M_{\text{dust}}$ . At  $z \sim 6.3$ , the dust mass in the most massive (CR) galaxy has reached  $M_{\text{dust}} \sim 4.1 \times 10^8 M_{\odot}$ . The sSFR and the dust mass in our massive (CR) galaxies are similar to those observed in SMGs at  $z \sim 3$  (e.g., Hatsukade et al. 2011; Michałowski et al. 2012). They appear only slightly smaller than in the bright SMG at  $z = 6.3$  discovered by Riechers et al. (2013), which has  $\text{SFR} \sim 2900 M_{\odot} \text{ yr}^{-1}$ ,  $M_{\text{star}} \sim 3.7 \times 10^{10} M_{\odot}$ , and  $M_{\text{dust}} \sim 1.3 \times 10^9 M_{\odot}$ . The most massive galaxy in our simulations has similar stellar and dust masses, but its SFR is smaller by a factor less than 4. Given the uncertainties in modeling the SF process, this is a very reasonable correspondence.

### 3.2 UV properties of galaxies

The UV continuum photons are overwhelmingly emitted by young stars (in the absence of the AGN). Some of them are absorbed by the dust before escaping from galaxies. Therefore, the galaxy UV properties are determined by their physical properties shown in Figure 3.

The calculated escape fraction,  $f_{\text{esc}}$ , of the UV photons in the  $\lambda = 1300 - 2000 \text{ \AA}$  band for the CR and UCR galaxies is displayed in the Figure 4. We find that most of the UV photons in galaxies with  $M_{\text{star}} \gtrsim 10^8 M_{\odot}$  have been absorbed by dust already at high redshifts,  $z \sim 12$ . Their photon escape fraction is  $f_{\text{esc}} \lesssim 0.1$  at this redshift and decreases further with the stellar mass. This mass dependence is consistent with the previous works (e.g., Yajima et al. 2011, 2014a), and the values at  $z = 7$  are similar to the published ones (e.g., Kimm & Cen 2013).

Figure 4 shows that  $f_{\text{esc}}$  is increasing towards smaller redshifts for galaxies with  $M_{\text{star}} \lesssim 10^9 M_{\odot}$ , while for higher-mass objects this increase is marginal. As a result, the me-

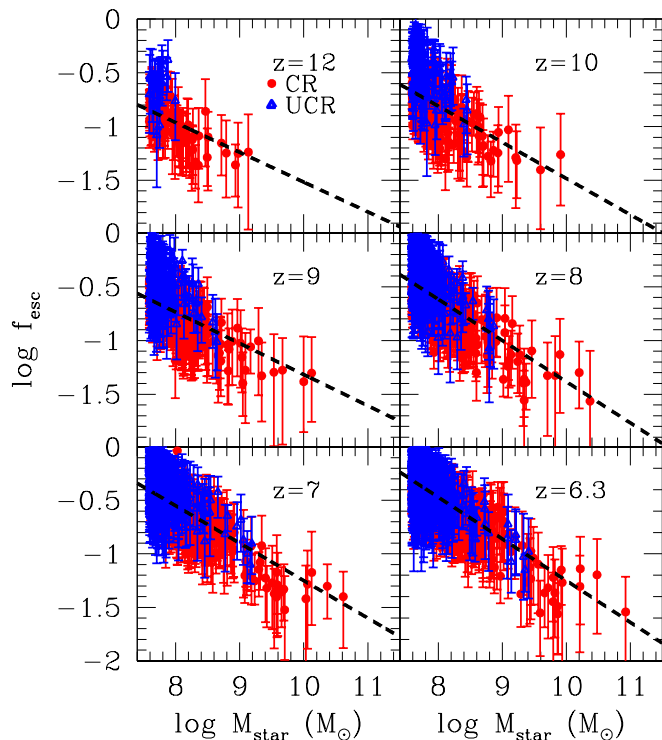


**Figure 4.** The calculated photon escape fraction,  $f_{\text{esc}}$ , at  $1300 \leq \lambda \leq 2000 \text{ \AA}$  in the rest-frame of the galaxy.  $f_{\text{esc}}$  is obtained by exact RT calculations and each point represent a galaxy in the CR and UCR samples (see text). The dashed lines represent the fits to the median values at each mass-bin with the bin-size of 0.5 dex, by using an equation shown in Table 2. The error-bars provide  $1\text{-}\sigma$  standard deviations for different viewing angles. Here, 50 angular bins have been used, 5 in  $\theta$  and 10 in  $\phi$ .

dian slope steepens with time. Dashed lines fit the median values with the mass bin of 0.5 dex using the fitting function,  $\log f_{\text{esc}} = \alpha \log M_{\text{star}} + \beta$ , where  $\alpha$  and  $\beta$  are the fitting parameters. The slope  $\alpha$  ranges from  $\sim -0.28$  to  $\sim -0.39$ .

The benchmark value of  $f_{\text{esc}} \sim 0.1$  moves to the right and is located at  $M_{\text{star}} \sim 3 \times 10^9 M_{\odot}$  by  $z \sim 6$ . The parameter  $\beta$  evolves from 1.25 at  $z = 12$  to 2.65 at  $z = 6.3$ . For galaxies with  $M_{\text{star}} \sim 10^{10} M_{\odot}$ , the  $f_{\text{esc}}$  increases from 0.03 to 0.06 during  $z \sim 10 - 6.3$ , while for  $M_{\text{star}} \sim 10^8 M_{\odot}$  galaxies it rises by a factor of 3. Hence galaxies become more transparent at lower  $z$  in our simulations, and low-mass galaxies show a more pronounced trend in this direction.

The  $f_{\text{esc}}$  in our simulations is smaller than that of Dayal et al. (2013). These authors have assumed that dust is distributed in a screen with a radius of  $0.225 R_{200}$  where  $R_{200}$  is the halo virial radius, taking the mean density of the sphere to be 200 times the critical density at a particular redshift. On the other hand, in our simulations, the gas distribution is clumpy, is found near the starforming regions, and, therefore, absorbs the stellar radiation more efficiently, resulting in lower  $f_{\text{esc}}$ .

The observed LBGs indicate a very high escape fraction because of the blue colours in the UV bands (e.g., Bouwens et al. 2010; Dunlop et al. 2013). In comparison, the  $f_{\text{esc}}$  of high-mass end galaxies in our simulations ap-

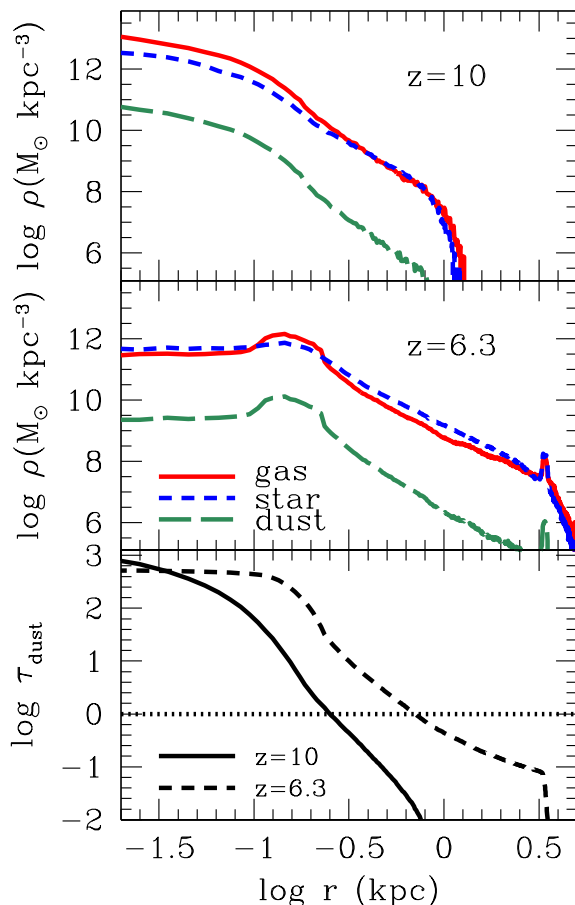


**Figure 5.** *Upper/middle:* The mean densities of gas, stars, and dust as a function of the radial distance from the galactic centers in physical coordinates. The samples consist of the most massive galaxies in the CR run at  $z = 6.3$  and 10. *Lower:* Optical depth of the dust calculated from the DM halo radius identified by the HOP group-finder algorithm, to a specific radius, using density distributions of the upper and middle panels.

pears smaller. By  $z \sim 6.3$ , our most massive CR galaxies with  $\sim 10^{11} M_{\odot}$  have  $f_{\text{esc}} \sim 0.03$ . Note that the estimated higher  $f_{\text{esc}}$  in the observed LBGs result from the assumed smooth dust extinction curve of local starforming galaxies from Calzetti et al. (2000). However, if one accounts for the bump at  $\lambda = 2175 \text{ \AA}$  in the dust extinction curve, the blue colour could still be obtained, despite  $f_{\text{esc}}$  being small.

Massive CR galaxies are compact, and have large amount of dust due to the high SFR. The stellar distributions are centrally concentrated, and the galactic centers — the sites of the SF — appear to be enshrouded in dust. Hence, the stellar radiation is efficiently absorbed. We note, that there is uncertainty in  $f_{\text{esc}}$  when using the UV colour alone, because the change in the UV colours by the dust extinction depends sensitively on the dust properties, e.g., its size and composition. If the typical grain size is smaller than that in the Milky Way, and the main component is graphite, the dust extinction does not change the UV colour or make

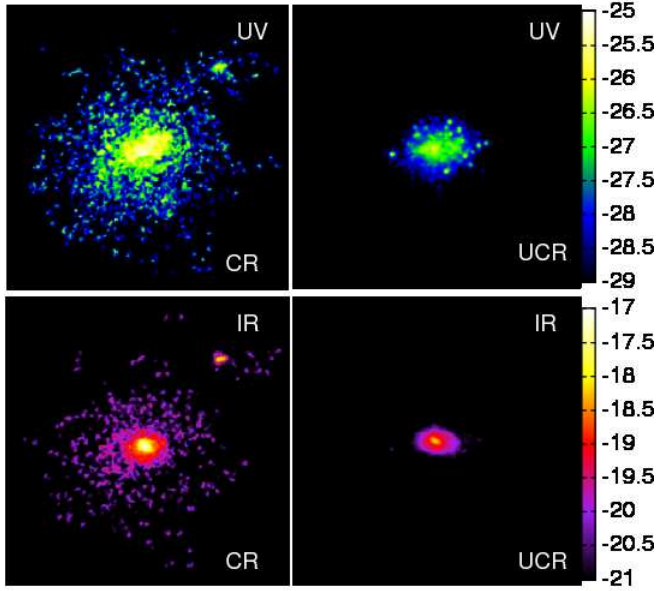


**Figure 6.** The surface brightness of the most massive galaxies in the CR (left column) and UCR runs (right column) at  $z = 6.3$ . Each panel size is the same as in the Figure 2. The upper panels show the UV band ( $\lambda \sim 1600 \text{ \AA}$  in the rest frame), which corresponds to the  $J$  band in the observed frame. The lower panels display the IR band ( $\lambda \sim 106 \mu\text{m}$ ), which corresponds to the sub-millimetre band of  $\lambda \sim 850 \mu\text{m}$ . The colours indicate the surface brightness in the log scale in units of  $\text{erg s}^{-1} \text{cm}^{-2} \text{Hz}^{-1} \text{arcsec}^{-2}$ .

it bluer because of the bump at  $\lambda = 2175 \text{ \AA}$  in the dust extinction curve (Inoue et al. 2006; Kimm & Cen 2013).

The most significant difference in  $f_{\text{esc}}$  between the CR and UCR galaxies, less than a factor of 2, can be seen in the lowest mass bin,  $M_{\text{star}} \sim 10^{7.5} - 10^{8.5} M_{\odot}$ , as we discuss in Section 3.5. The reason for this is that the gas distribution, and hence the distribution of SF regions and dust, in the CR galaxies are more compact than in the UCR ones. As shown in Romano-Díaz et al. (2014), the galaxies in a particular mass range form earlier in overdense regions, compared to ‘normal’ regions in the universe. This happens because the accretion rate depends on the background density in addition to the halo/galaxy mass. Indeed, in our simulations, the low-mass galaxies in CR form earlier than the UCR ones, resulting in a more compact gas/star distribution and a more efficient dust extinction. At earlier times, the universe is denser and the parent DM halos have larger concentration parameter, causing compact gas distribution.

The radial distribution of the gas, stars and dust in the CR run are shown in Figure 5. We take the most massive galaxies at  $z = 6.3$  and  $10$ , and estimate the mean density in spherical shells at each radius. Most of them are distributed in the central kiloparsec. Half-mass radii of the gas are  $95 \text{ pc}$  at  $z = 10$  and  $215 \text{ pc}$  at  $z = 6.3$ . Due to the compact distributions, the optical depth at  $\lambda = 1300 \text{ \AA}$ , estimated from the boundary of the grid placed around each galaxy to an arbitrary radius  $r$ , i.e.,  $\tau(r) = \int_{\text{boundary}}^r \sigma_{1300} \rho_{\text{dust}}(r) dr$ , increases steeply when approaching the galactic centre. At  $z = 10$ , the optical depth to  $r \lesssim 0.25 \text{ kpc}$  is larger than unity, and this radius increases to  $r = 0.71 \text{ kpc}$  at  $z = 6.3$ . The stellar distribution behaves similarly. For example, the mass

$\sim 0.8 M_{\text{star}}$  is within the radius mentioned above, where the ISM is optically thick at  $z = 10$ , but decreases somewhat to  $\sim 0.68 M_{\text{star}}$  at  $z = 6.3$ .

Consequently, most of the stellar UV radiation is absorbed by the dust. Note, that, despite lower dust mass at  $z = 10$ , the fraction of stellar mass inside the radius of  $\tau = 1$  is higher than that at  $z = 6.3$ , due to the compact dust and stellar distributions. Therefore, even at high redshifts, stellar UV radiation of galaxies residing in the overdense regions can be absorbed by the dust. The gas and dust appear to be pushed away from the center at lower redshifts.

The surface brightness of the most massive galaxies in the CR and UCR runs at  $z = 6.3$  is shown in  $J$  and sub-millimetre bands (Figure 6). The  $J$  band in the observed frame corresponds to the UV band in the rest frame. The  $J$ -band flux of the galaxy in the CR run exhibits a similar distribution to the stellar one (Figure 5), e.g., 1-D radial distribution. However, some parts get fainter, because of the stronger dust absorption. On the other hand, the sub-millimetre flux traces the dust distribution, and, therefore, is more compact compared to the  $J$ -band flux. The  $J$  and sub-millimetre band fluxes of the galaxy in the UCR run show similar distributions reflecting stars and dust, respectively. However, the UV flux is flatter compared to the stellar distribution, and the sub-millimetre flux is more compact due to the effect of the radiative transfer, i.e., UV flux near the galactic centers is efficiently absorbed, as shown in Figure 5.

The UV fluxes from galaxies at  $\lambda \sim 1300 \text{ \AA}$  in the rest frame are shown in Figure 7. The flux is the angular mean. Dotted and dashed lines represent fitting lines to median values with the mass bin of  $0.5$  dex, using the function  $m_{\text{UV}} = \alpha \log M_{\text{star}} + \beta$ . For the intrinsic  $m_{\text{UV}}$ ,  $\alpha \sim -2.3$ , which means that the UV flux increases linearly with the stellar mass,  $M_{\text{star}}$ , since  $m_{\text{UV}} \propto -2.5 \log F_{\nu}^{\text{UV}}$ , where  $F_{\nu}^{\text{UV}}$  is the UV flux density. This happens because the UV flux is proportional to the SFR (Kennicutt 1998a) which correlates with the stellar mass, as shown in Figure 3. On the other hand, due to the mass dependence of  $f_{\text{esc}}$ , the fitting lines to  $m_{\text{UV}}$  are flatter with  $\alpha \sim -1.3$ , considering the dust extinction. Hence, after correction by the dust extinction,  $F_{\nu}^{\text{UV}} \propto M_{\text{star}}^{0.52}$ .

We find that, before the dust extinction has been applied, many CR galaxies appear above the detection threshold for recent observations of the Hubble Ultra-Deep Field (HUDF) with the Wide-Field Camera 3 (WFC3) onboard the HST (Bouwens et al. 2011). However, due to the strong dust extinction, the galaxies in the CR run become fainter by  $\sim 5$  magnitudes. As a result, many of the galaxies appear below the detection threshold for the current HST observations. At  $z \sim 10$ , only a few bright galaxies appear above the threshold. In the UCR run, the intrinsic UV fluxes of most galaxies are fainter than the detection threshold at  $z \gtrsim 8$ . Only a few galaxies at  $z \lesssim 7$  can be observable as LBGs.

The error bars in Figure 7 show the dispersion in  $m_{\text{UV}}$  due to the viewing angle. Because of the anisotropic stellar and dust distributions, the UV flux changes significantly. On average, the dispersion increases with the stellar mass, because the galaxy shapes become more disk-like (see § 3.6, and also Romano-Díaz et al. 2011b; Biffi & Maio 2013), and the photons escape efficiently along the normal direction to the disk plane. This can affect significantly the limiting CR galaxy mass, moving it by about a decade in  $M_{\text{star}}$ , from



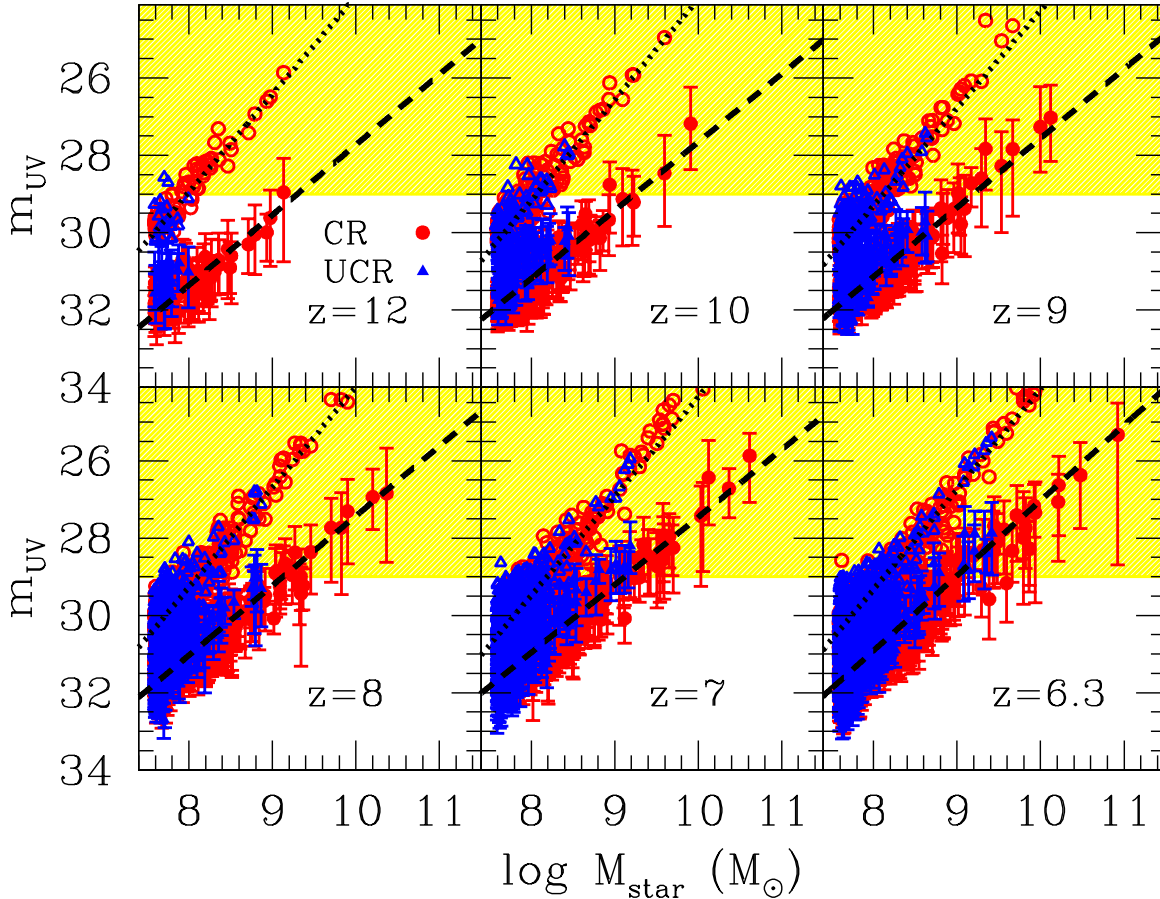


**Figure 7.** The UV flux density in AB magnitudes as a function of stellar mass,  $M_{\text{star}}$ . The yellow shades show the detectable region ( $m_{\text{UV}} \sim 29$  mag) in the recent observations using the HST (e.g., Bouwens et al. 2011). The red and blue symbols show galaxies in the CR and UCR runs respectively. Filled and open symbols represent the UV fluxes with and without the dust extinction. The error bars of the filled circles represent the minimum and maximum values of the different viewing angles of a galaxy. The dotted and dashed lines are fitting lines to the median values with a bin size of 0.5 dex with and without the dust extinction, when applying the fitting function  $m_{\text{UV}} = \alpha \log M_{\text{star}} + \beta$ , where  $\alpha$  and  $\beta$  are the fitting parameters (see text).

$\sim 10^9 M_{\odot}$  to  $\sim 10^{10} M_{\odot}$ . For example,  $m_{\text{UV}}$  of the most massive galaxy at  $z = 6.3$  in the CR ranges from 24.5 to 28.7. Therefore, for many galaxies, the detection by the HST depends on the viewing angle. Since the dust absorption cross section decreases with increasing wavelength, dispersion becomes smaller at longer wavelengths. This effect may cause variation of physical properties in observational study using the SED fitting. We shall discuss additional details in Section 4.

Recently, Stark et al. (2013) estimated the relation between stellar mass and  $M_{\text{UV}}$  at  $z \sim 4-7$ . Figure 8 shows the relationship between the stellar masses of galaxies and their emerging UV flux in our simulations at  $z = 7$ , corrected and uncorrected for the dust attenuation. Stellar masses in the UCR galaxies lie within the range estimated by these observations. Because the UCR run is using a small volume, we cannot sample larger galaxies, because they are rare and difficult to find in such volumes (see Section 2). The stellar masses of our CR galaxies with  $M_{\text{UV}} > -18$  exceed those of Stark et al. by a factor of a few, while the dimmer ones fall within the observed range. We note that the CR

galaxies reside in the highly overdense region which tends to evolve ahead of the average density regions in the universe. For example, their SF starts at higher redshifts than in the UCR galaxies. As a result, a larger fraction of the UV photons will be attenuated by larger amount of dust, and the stellar mass-to-emerging UV flux ratio becomes higher in comparison with the observed LBGs. Our numerical model implementation has also successfully reproduced the cosmic SFR density, the metal abundance in the IGM (e.g., Choi & Nagamine 2009), and the neutral hydrogen abundance (e.g., Nagamine et al. 2010a; Yajima et al. 2012d). Furthermore, observations of stellar masses in galaxies include uncertain parameters, such as ages, star formation history, dust extinction, and nebular emission lines in the SED fitting. These parameters could change the estimated values of stellar masses significantly, and make it more in agreement with our CR models. Given these considerations, we conclude that the stellar masses of our simulated galaxies are in reasonable agreement with those observed by Stark et al. (2013).

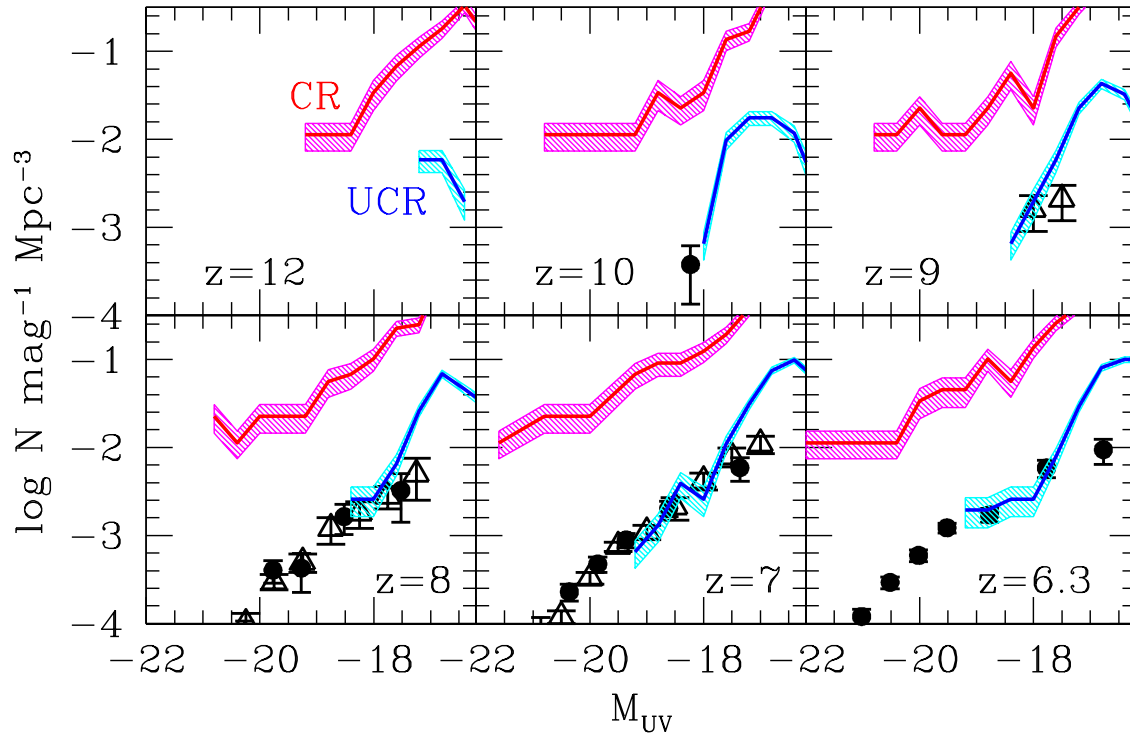


**Figure 9.** The galaxy UV luminosity function after applying the dust correction (see text). The red and blue lines represent the simulation results for the CR and UCR runs, respectively. The shaded regions represent the Poisson errors. Filled circles and open triangles are observational data by Bouwens et al. (2014b) at  $z = 6, 7, 8$ , and 10, and McLure et al. (2013) at  $z = 7, 8$ , and 9, respectively.

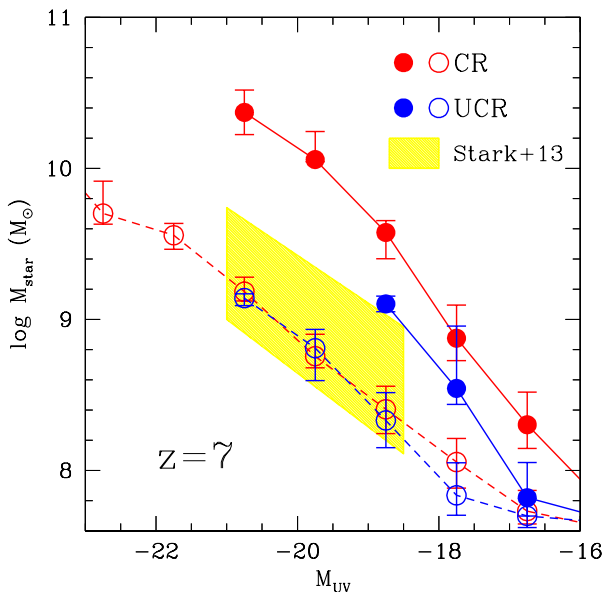


**Figure 8.** Stellar masses of galaxies as a function of the rest-frame UV magnitude at  $z=7$ . Filled and open circles represent median values of galaxies with corrected and uncorrected UV fluxes by dust extinction, respectively. The yellow shaded region shows the observed galactic stellar masses accounting for the ambiguity from the contribution by the nebular lines from Stark et al. (2013).

### 3.3 UV luminosity function of galaxies

Galaxy luminosity functions (LFs) range has been extended recently to  $z \gtrsim 8$  from observations in the UDF, GOODS-N, GOODS-S and the XDF fields (Bouwens et al. 2014b). Moreover, using the UKIDSS field, few candidates have been detected also at  $z \gtrsim 9$  (McLure et al. 2013, see also Oesch et al. 2013). This enables us to compare our simulation results to the observed LFs as shown in Figure 9.

Since the CR simulation has been performed in a targeted, highly overdense environment of a  $5\sigma$  region, the number densities of galaxies are substantially higher than the mean ones probed by the observations. At present, the Constrained Realization method constitutes an elegant way to sample such statistically rare regions without any loss of generality, compared to the use of large-scale simulations with re-sampling.

On the other hand, we also demonstrate that the LF in the UCR run nicely agrees with the observed LFs at the fainter side. Without the dust extinction (not shown here), the LFs are shifted a few magnitudes brighter, and hence deviate from the observed ones. These shifts are related to  $f_{\text{esc}}$  through  $M_{\text{UV}} - M_{\text{UV}}^{\text{int}} = -2.5 \log f_{\text{esc}}$ . Therefore,  $M_{\text{UV}}$  of massive CR galaxies with  $f_{\text{esc}} < 0.1$  becomes fainter by more than 2.5 magnitudes, while that of the low-mass UCR galaxies with  $f_{\text{esc}} > 0.3$  shifts down by less than 1.3 magnitudes.

This result is interesting and of a prime importance to observations of high-redshift galaxies, as it shows that the dust extinction is important in the  $z \gtrsim 6$  galaxies. We note

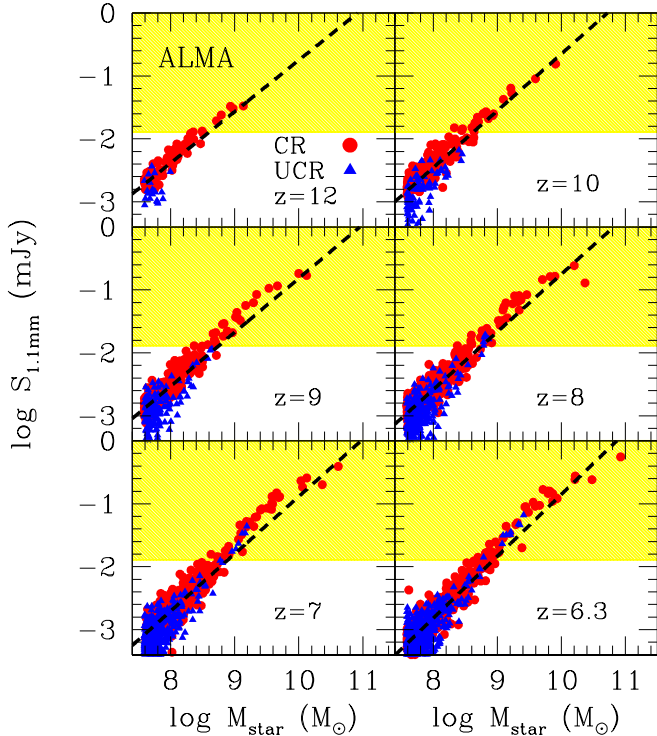


**Figure 10.** The sub-millimetre flux at  $\lambda = 1.1$  mm in the observed frame. The yellow shades show the region of  $S_{1.1\text{mm}} > 0.013$  mJy, which corresponds to the detection threshold of ALMA with  $\sim 1$  hour integration using 50 12-m antennas.

that due to a relatively small computational box for the UCR galaxies, it does not include massive bright galaxies with  $L > L^*$ . Hence, our results in the UCR run are limited at  $m_{\text{UV}} \gtrsim -19$ .

The reasonable agreement of the UCR LF with observations after the dust extinction correction also provides support to the CR run results, which has been performed with the same physical models, except for the environment of higher densities. We note that, if quasars indeed reside in such massive galaxies, their spatial distribution will reflect the distribution of our CR galaxies in the sky with the limited volume, accounting for quasar duty cycle somewhat smaller than unity.

Our results indicate that even galaxies at  $z \gtrsim 6$  can suffer from the dust attenuation. On the other hand, recent observations have shown that the slope  $\beta$  of the UV flux is  $\sim -2$  (e.g., Dunlop et al. 2012). If we consider the smooth dust extinction curve, such as the Calzetti law (Calzetti et al. 2000),  $\beta \sim -2$  means that the dust attenuation is small (Meurer et al. 1999). However, the SNe dust model is associated with the extinction curve which exhibits a bump at  $2175 \text{ \AA}$ , due to the small graphite dust. Therefore, our SNe dust model does not increase  $\beta$  with the dust extinction, i.e., the dust extinction  $A_{\text{UV}}$  is nearly independent of this parameter (e.g., Figure 1 in Yajima et al. 2014b). This is unlike the relation between the dust extinction and the slope  $\beta$  in the local starforming galaxies (Meurer et al. 1999). We confirm that even galaxies with a strong dust extinction keep  $\beta \sim -2$ , which is nearly the value of the intrinsic SEDs. We

also note that the UV slope through broad-band filters can change significantly by the contribution from nebular lines (e.g., Schaerer 2003; Schaerer & de Barros 2009), which is not included in our current simulations.

### 3.4 Infrared properties of galaxies and detection by ALMA

Dust absorption of the stellar radiation leads to the dust thermal emission in the infrared band, in the galaxy’s rest frame. This emission from the high-redshift galaxies is bright in the sub-millimetre band of the observed frame. Figure 10 displays the sub-millimetre fluxes at 1.1 mm, hereafter  $S_{1.1}$ . The SFR and the dust mass increase linearly with the galactic stellar mass as seen in Figure 3. Most of the stellar radiation is absorbed, therefore, it leads to the increasing sub-millimetre and the IR luminosity,  $L_{\text{IR}}$ , with increasing  $M_{\text{star}}$ . The most massive galaxies in the CR run have  $L_{\text{IR}} \sim 6.3 \times 10^{11} L_{\odot}$  at  $z \sim 10$  and  $3.7 \times 10^{12} L_{\odot}$  at  $z = 6.3$ . The dash lines are fitted to median values with the mass bin of  $\Delta \log M_{\text{star}} = 0.5$ , using a function  $\log S_{1.1} = \alpha \log M_{\text{star}} + \beta$ . The IR luminosity displays a similar slope to that of the SFR, namely  $L_{\text{IR}} \propto M_{\text{star}}^{1.1}$ . This happens because the UV luminosity, which is given by the SFR, is nearly all converted into  $L_{\text{IR}}$ . On the other hand, the slope of  $S_{1.1}$  shows a shallower  $\alpha \sim 0.9$ , because  $\lambda = 1.1$  mm lies at the long-wavelength tail of the thermal peak of the dust emission. For example, the peak wavelength of IR radiation from the most massive galaxy is  $\sim 300 \mu\text{m}$ , while that of the observed SMG shows  $\sim 500 \mu\text{m}$ . Therefore, when the dust temperature increases with increasing  $L_{\text{IR}}$ , the peak intensity moves to smaller  $\lambda$  and becomes higher. Hence the increase in the intensity around the peak is larger than in the tail. For a fixed covering area of dust emission, this translates into slower increase in the IR flux at the tail, compared to  $L_{\text{IR}}$ .

The detection threshold by the recent ALMA observations is  $S_{1.1} \sim 0.013$  mJy, which corresponds to  $\sim 1$  hour integration with 50 12-m antennas. Even at  $z = 8$ , the galaxies in the UCR run appear undetectable because of the lower SFR. On the other hand, massive galaxies in the CR run can be easily detected by ALMA up to  $z \sim 10$ .

The massive galaxies in CR run appear fainter than the observed SMG at  $z = 6.3$  by factor  $\sim 10$  (Riechers et al. 2013), although the stellar and dust masses are similar. There are at least three options which can explain such a difference. First, the observed SMG could be detected during an extreme starburst phase, while our model galaxies mostly evolved with smooth gas accretion (Romano-Díaz et al. 2014). Second, the CR galaxies could have a different dust covering factor of the central SF sites. Alternatively, the modelled and observed galaxies can lie in different environments, which lead to different accretion rates, gas fractions, etc. Note that the number of detected SMGs at  $z \gtrsim 6$  is still quite small. Future surveys of high-redshift SMGs using ALMA will allow for a better and statistically significant comparison.

While we focus on the dust continuum emission in this work, we note that the metal lines, e.g., C and O, and the CO molecular lines enhance the detectability of high-redshift galaxies (e.g., Inoue et al. 2014; Tomassetti et al. 2014).

### 3.5 Redshift evolution of galaxies

The dust mass increases with time as well as with the SF (Figure 3), and the dust distribution around the star-forming regions changes with time as well (Figure 5). Consequently, the spectral properties of galaxies are expected to evolve with redshift. Figure 11 shows the redshift evolution of  $f_{\text{esc}}$  and the  $S_{1.1}$  flux. The symbols represent the medians in galaxies in each mass range. Because of a higher number of low-mass galaxies in the galaxy mass function, the median values are similar to those of low-mass samples ( $10^{7.6} < M_{\text{star}} \leq 10^{8.5} M_{\odot}$ ). This effect dominates the UCR run because the massive galaxies are completely absent there. The median values increase with decreasing redshift, despite of the increase in the dust amount.

As shown in Figure 5, at higher redshift, the dust is distributed compactly around the starforming region at the galactic centre. Therefore, smaller amounts of dust can efficiently absorb the stellar radiation, resulting in the suppression of  $f_{\text{esc}}$ . As we have discussed in Section 3.3,  $f_{\text{esc}}$  of the CR galaxies in the lowest mass bin lies below that of the UCR one, by less than a factor of 2 (see Figure 11). The photon escape fraction,  $f_{\text{esc}}$ , of the high-mass galaxies with  $M_{\text{star}} \gtrsim 10^{9.5} M_{\odot}$ , does not change much. These galaxies have extended disks even at high redshift of  $z \gtrsim 10$  (Romano-Díaz et al. 2011b), hence photons can escape from stars at the outskirts of a galaxy.

The bottom panels show the redshift evolution of  $S_{1.1}$ . Although  $L_{\text{IR}}$  increases with decreasing redshift because of the higher SFR,  $S_{1.1}$  does not change significantly. Due to an increase in the dust temperature with  $L_{\text{IR}}$ , the  $S_{1.1}$  flux is nearly constant. Only massive galaxies with  $M_{\text{star}} \gtrsim 10^{9.5} M_{\odot}$  show an increase in  $S_{1.1}$  by a factor of 2 between  $z \sim 12$  and 10, and can be detected by ALMA, while most galaxies are too faint with  $S_{1.1} \lesssim 10^{-2}$  mJy.

### 3.6 Effect of the galactic morphology on the spectral properties

Escape of the UV continuum photons from galaxies is sensitive to the viewing angles due to the anisotropic column densities, as shown in Figures 4 and 7. Here we investigate the effect of galaxy morphology on the dispersion of  $f_{\text{esc}}$ . We define the three galactic semi-axes as  $a$ ,  $b$  and  $c$  from the inertia tensor, with  $a > b > c$  (Heller et al. 2007).

The relation between  $c/a$  and stellar mass is shown in Figure 12. No clear correlation can be seen for  $M_{\text{star}} \lesssim 10^8 M_{\odot}$  for the CR and UCR runs. Only the CR run shows that  $c/a$  of massive galaxies decreases roughly with increasing stellar masses. This can be directly related to the high accretion rate of cold gas from cosmological filaments around high-density peaks, which tends to form an extended disk (see also Romano-Díaz et al. 2014). These disks appear to be resilient (Romano-Díaz et al., in preparation). In addition, the dispersion becomes large for  $M_{\text{star}} \gtrsim 10^9 M_{\odot}$  again, this might be due to merging processes.

Then we measure the  $1\sigma$  error in  $f_{\text{esc}}$  by different viewing angles,  $\sigma_{\text{esc}}$ , normalised by the angular mean  $f_{\text{esc}}$  of each galaxy, as a function of  $c/a$ . Figure 13 displays the median values of each redshift sample. Since most galaxies with  $M_{\text{star}} \gtrsim 10^9 M_{\odot}$  show  $c/a \ll 1$  (and  $a \sim b$ ), this leads to a verifiable conclusion about the presence of geometrically-

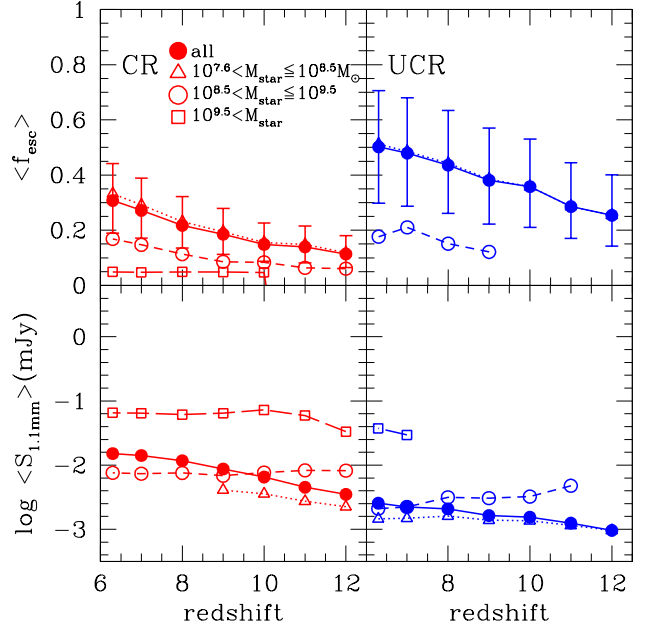


**Figure 11.** *Upper:* Redshift evolution of the UV escape fraction  $f_{\text{esc}}$ . Filled symbols represent the median values of the full sample, open symbols are the means in each mass bin. Red and blue colours represent the CR and UCR runs, respectively. Note that red and blue triangles follow the “all” red and blue filled circles. The error bars are the quartiles of the sample in each mass bin. *Lower:* Redshift evolution of the quartiles of the sub-millimetre flux  $S_{1.1}$  at 1.1 mm in the observed frame.

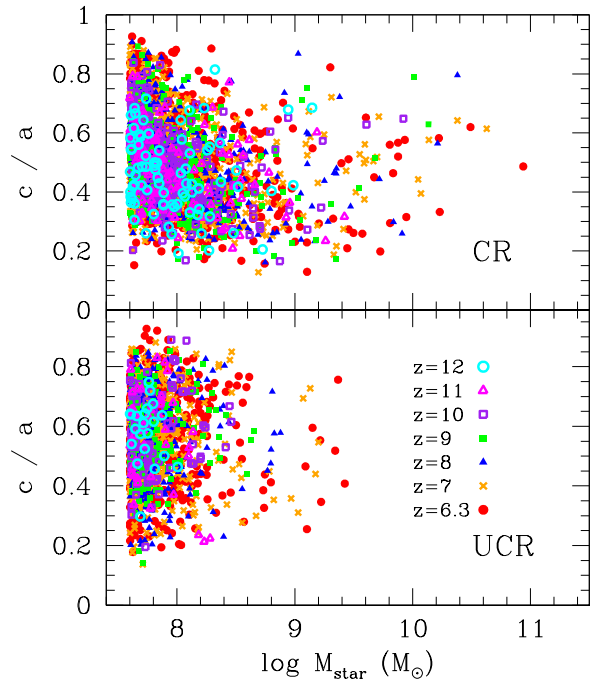


**Figure 12.** The axial ratio ( $c/a$ ) as a function of stellar mass for the CR and UCR runs. See definitions of the galactic semi-axes,  $a$ ,  $b$ , and  $c$  in the text.

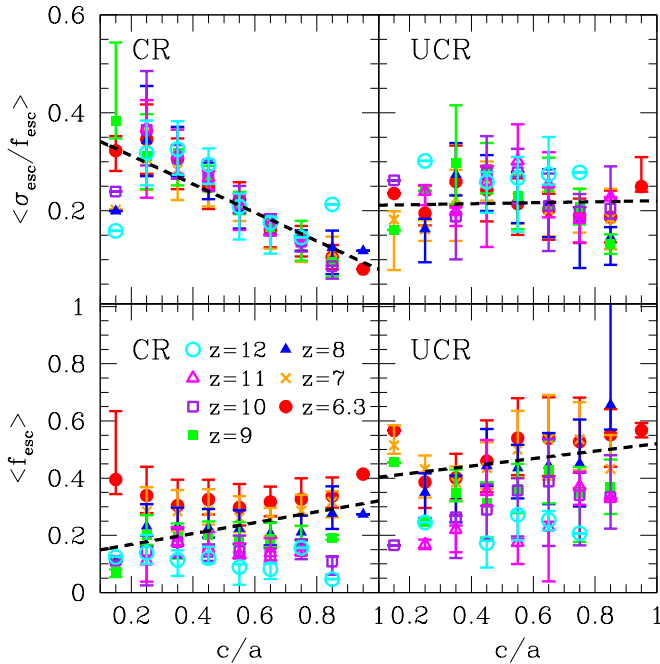


**Figure 13.** *Upper:* Coefficients of variation of the UV escape fraction for different viewing angles normalized by the angular mean values,  $\equiv \sigma / f_{\text{esc}}$ , as a function of the galactic axial ratio  $c/a$ . Symbols represent medians at each bin. The error bars are top and bottom quartiles. *Lower:* Escape fraction of the UV continuum photons as a function of  $c/a$ . The dash lines represent fit to the median values for all redshift samples by using a function  $\sigma_{\text{esc}}/f_{\text{esc}}$ , or  $f_{\text{esc}} = \alpha(c/a) + \beta$ , where  $\alpha$  and  $\beta$  are the fitting parameters.

thin disks in these objects. Spheroidal galaxies show  $c/a \sim 1$  and  $a \sim b$ . For the CR run, scatter in  $f_{\text{esc}}$  increases roughly with decreasing  $c/a$  (e.g., upper left frame in Figure 13). Photons can escape along the normal direction to the disk plane due to the lower column density.

The ratio  $\sigma_{\text{esc}}/f_{\text{esc}}$  ranges from  $\sim 0.35$  at  $c/a \sim 0.2$  to  $\sim 0.1$  at  $c/a \sim 0.8$ . The median values can be fit by  $\sigma/f_{\text{esc}} = -0.29 \times (c/a) + 0.37$ . On the other hand, for the UCR run, most galaxies are low-mass, and the optical depth along the edge-on disks is not so high. Therefore, even disk galaxies do not show large dispersion for the UCR run. Furthermore, some galaxies with  $c/a \sim 0.5$  have high  $\sigma_{\text{esc}}/f_{\text{esc}}$  and  $f_{\text{esc}}$ . We measure the Pearson’s correlation coefficient for all samples shown in the top panels of Figure 13, and obtain  $-0.66$  for the CR run and  $-0.18$  for the UCR run. This clearly shows that the correlation is stronger for the CR galaxies in the top-left panel.

The bottom panels of Figure 13 show  $f_{\text{esc}}$  as a function of  $c/a$ . Here,  $f_{\text{esc}}$  is the angle-averaged value, and each point represents one galaxy. There appears to be no clear correlation between the morphology and  $f_{\text{esc}}$ . The correlation coefficient is 0.03 for the CR run, and 0.20 for the UCR run, respectively. Thus, we conclude that the disk shape of massive galaxies causes the large dispersion in  $f_{\text{esc}}$  value, but does not change  $f_{\text{esc}}$  itself significantly. In our model galaxies, the high-density gas clumps are distributed around the star-forming regions, and efficiently absorb UV

photons. Hence,  $f_{\text{esc}}$  depends on the covering factor of the clumps, and  $\sigma_{\text{esc}}/f_{\text{esc}}$  is affected by the anisotropy in this distribution. Figure 13 shows that the anisotropy increases with decreasing  $c/a$ , but the covering factor does not depend on it significantly. For the disk and no-disk galaxies, photons emitted by stars far from the galaxy centers, escape efficiently. Yet, there is a preferred direction of escape for photons emitted close to the centers of disk galaxies, i.e., the normal direction to the disk plane, resulting in larger dispersion of  $f_{\text{esc}}$ .

## 4 DISCUSSION & SUMMARY

We used the high-resolution zoom-in cosmological simulations of galaxies by Romano-Díaz et al. (2011b, 2014) and have post-processed them with a 3-D radiation transfer code. We examined the evolution of multi-wavelength spectral properties of high-redshift galaxies. The spatial resolution in the comoving coordinates is  $\epsilon = 300 h^{-1} \text{pc}$ , which corresponds to (in physical coordinates)  $23 h^{-1} \text{pc}$  at  $z \sim 12$  and  $43 h^{-1} \text{pc}$  at  $z = 6$ . We used two different types of simulation setup. One simulated an unconstrained average region in the universe (the UCR run). Another simulation was prepared by imposing a constraint in order to simulate a rare, highly-overdense,  $5\sigma$  region in a cubic box of  $20 h^{-1} \text{Mpc}$ , which includes the seed of  $\sim 10^{12} h^{-1} M_{\odot}$  DM halo projected to collapse by  $z \sim 6$  (see Romano-Díaz et al. 2011b, 2014, for more details). This was prepared using the Constrained Realization (hereafter the CR run) method (Hoffman & Ribak 1991; Romano-Díaz et al. 2011a). Our simulations contain  $\sim 50 - 600$  galaxies  $M_{\text{star}} \gtrsim 4 \times 10^7 M_{\odot}$  for each of the seven representative snapshots during  $z \simeq 6.3 - 12$ . The total samples consist of 2273 galaxies for the CR run, and 1789 galaxies for the UCR run.

We find that, in the CR run, massive galaxies with  $M_{\text{star}} \sim 10^{11} M_{\odot}$  form within DM halos of  $\sim 1 - 2 \times 10^{12} M_{\odot}$  by  $z \sim 6$ , and such regions can serve as a hotbed for the formation of high- $z$  quasar hosts — the overall evolution in the overdense region has been accelerated dramatically with respect to the normal fields. Numerical simulations estimate that a comoving density of such massive DM halos exceeds the comoving density of high- $z$  quasars. Using the WMAP9 cosmological parameters (Hinshaw et al. 2013), we obtain about 200 such halos per  $1 h^3 \text{Gpc}^{-3}$ . This makes their comoving space density about 100 times above that of  $z \gtrsim 6$  quasars,  $\sim 2 h^3 \text{Gpc}^{-3}$  (e.g., Fan et al. 2003; Willott et al. 2010), if the duty cycle of these quasars is unity. For lower duty cycle, their space densities can be similar. The physical properties of these galaxies change significantly with their environment, leading to a different dust extinction, and therefore, to different spectral appearances. Much lower mass galaxies with  $M_{\text{star}} \lesssim 3 \times 10^9 M_{\odot}$  have been found in the average density run, but this lower limit of the galaxy mass is of course expected to increase for larger computational boxes with the same SPH mass resolution. With our goal of separating the environments of overdense and average regions in the universe, the adopted sizes of computational boxes are suitable to probe massive and low-mass star-forming galaxies for the current numerical resolution.

We find that galaxies in the CR and UCR simulations exhibit the following physical properties:

• The LFs for  $M_{UV} \gtrsim -19$  of the UCR galaxies at  $z \sim 6 - 10$ , processed with RT and dust extinction, have matched the observed LFs of Bouwens et al. (2014b) and McLure et al. (2013). This is an important test for the modelled galaxies. Other than the assumption that the dust size follows the SNe dust model and the dust distribution traces the metals and implying that the dust-to-metal mass ratio in these galaxies do not differ from those at low redshifts (but see Gallerani et al. 2010), no additional assumptions and no additional corrections have been made. It also implies that the dust extinction is important in high- $z$  galaxies, at least to  $z \sim 9$ , for our simulations. The LFs for the CR galaxies have been calculated for  $M_{UV} \gtrsim -19.5$  at  $z = 12$ ,  $M_{UV} \gtrsim -21$  at  $z = 8 - 10$ , and  $M_{UV} \gtrsim -22$  at  $z = 6.3$ , and overestimated the observations because of the biased high-density region.

• The escape fraction of the non-ionizing UV photons,  $f_{esc}$ , decreases with increasing stellar mass. Massive galaxies with  $M_{star} \gtrsim 10^{9.5} M_{\odot}$  exhibit  $f_{esc} \lesssim 0.1$ , and show little redshift evolution. While the low-mass galaxies with  $M_{star} \lesssim 10^{8.5} M_{\odot}$  show a strong redshift evolution, and increase  $f_{esc}$  from  $\sim 0.1$  at  $z \sim 12$  to  $\gtrsim 0.3$  at  $z \sim 6.3$ . We show that the CR galaxies can be easily detected by the current observations with the HST at  $z \lesssim 10$ , and some of the most massive UCR galaxies can be detected for  $z \lesssim 7$ . We find that the emerging UV flux from galaxies increases linearly with  $M_{star}$ , but due to the mass dependence of  $f_{esc}$ , the increase rate becomes much slower, i.e.,  $F_{\nu}^{UV} \propto M_{star}^{0.52}$ .

• The most massive CR galaxies have IR luminosities of  $L_{IR} \sim 6 \times 10^{11} L_{\odot}$  at  $z \sim 10$ , and  $\sim 4 \times 10^{12} L_{\odot}$  at  $z \sim 6.3$ , and  $L_{IR} \sim M_{star}^{1.1}$ . Massive galaxies appear bright at the sub-millimetre band because of the high SFR  $\gtrsim 100 M_{\odot} \text{ yr}^{-1}$ , and a strong dust extinction,  $f_{esc} \lesssim 0.1$ . The 1.1 mm flux exhibits a weaker dependence on  $M_{star}$  than  $L_{IR}$ , i.e.,  $S_{1.1} \sim M^{0.9}$ . This flux is  $\gtrsim 10^{-2}$  mJy, and hence massive high-redshift galaxies can be detected by ALMA up to  $z \sim 10$ . On the other hand, most of the UCR galaxies are difficult to detect by ALMA due to the lower SFR and dust amount. The fluxes of metal lines of C and O, and the CO molecular lines can be higher than the continuum emission from dust, and may enhance their detectability (Inoue et al. 2014), although the physical state of the metals (e.g., their ionization levels and molecular fractions) are not clear.

• Some galaxies show disk shapes, which causes the large dispersion in the emerging UV flux depending on the viewing angle. Massive galaxies tend to be disk due to the efficient gas accretion from the IGM.

• The SFR, stellar mass, dust mass and other parameters of our massive CR galaxies agree broadly with the observed SMGs at  $z \sim 3$  (e.g., Hatsukade et al. 2011), and they correspond roughly to the bright SMG at  $z = 6.3$ , discovered by Riechers et al. (2013), which exhibits SFR  $\sim 2900 M_{\odot}$ ,  $M_{star} = 3.7 \times 10^{10} M_{\odot}$  and  $M_{dust} \sim 1.3 \times 10^9 M_{\odot}$ .

The observed properties of high-redshift galaxies have been used to determine their intrinsic properties and to constrain the ongoing physical processes. One of the most important parameters appears to be the escape fraction of the UV photons, both ionizing and non-ionizing. Here we focused on the latter one and determine its effect on the measurable quantities, like the attenuated UV flux and the galaxy luminosity function. This has been done comparing

the normal and substantially overdense regions in the universe. We did not find any substantial differences between the CR and UCR runs, except those which can be directly linked to the environmental contrast, i.e., the background density. The associated accelerated growth of the CR galaxies can indeed produce the massive quasar hosts by  $z \sim 6$ . Their LF appears to exceed that of the UCR galaxies by a factor of 10–50 already at  $z \lesssim 12$ , and to extend to the absolute magnitudes of  $\sim -22$  by  $z \sim 6$ .

We have applied the SN dust model (Todini & Ferrara 2001) and the constant dust-to-metal mass ratio based on the observations of local star-forming galaxies (Draine et al. 2007). On the other hand, dust properties of high-redshift galaxies are not understood yet, and there is still room for varying the dust size, composition, and the dust-to-metal mass ratio. Different dust models lead to distinct opacity curves as a function of wavelength, resulting in the different spectral properties (Yajima et al. 2014b). However, if photons are mainly absorbed by the high-density clumps,  $f_{esc}$  and emerging  $m_{UV}$  are not sensitive to the dust models. This ensues because most of the photons crossing these clumps are absorbed regardless of the dust properties within reasonable parameter ranges (Yajima et al. 2014b). In this case,  $f_{esc}$  and  $m_{UV}$  are determined mainly by the covering factor of the gas clumps. On the other hand, the IR properties of the emerging radiation can vary with the dust temperature dependence on the grain size (Cen & Kimm 2014). At present, it is hard to constrain the dust temperature in galaxies at  $z \gtrsim 6$  from the observational data, because of the difficulty to detect sub-millimetre fluxes at several frequencies.

Recently, Kimm & Cen (2013) and Cen & Kimm (2014) investigated UV and IR galaxy properties in overdense region at  $z = 7$ , by using cosmological adaptive mesh refinement (AMR) simulations and radiative transfer calculations. They have shown that  $M_{star} \sim 5 \times 10^8 - 2.5 \times 10^{10} M_{\odot}$  galaxies have been heavily dust obscured and their UV properties could be modified by the dust models. We have obtained similar results for  $z = 7$ , however, our larger sample extending over a substantial range in redshift, as well as dramatically larger range of environment by considering the CR run, and therefore of the galaxy masses, allow to analyze the redshift evolution and detailed mass dependence of the observational properties of high-redshift galaxies, and the impact of galaxy morphology on their observational appearance. In addition, although our simulations have shown strong extinction, the slope  $\beta$  in  $F \propto \lambda^{\beta}$  does not increase. This happens because of the presence of a bump at  $\lambda \sim 2175 \text{ \AA}$  (Li et al. 2008) in our dust model of type II SN. Similar results have been obtained also by Kimm & Cen (2013). A large parameter space in dust properties should be considered in the future studies and constrained by observations.

The overall mass range of galaxies in the UCR run and the lower mass galaxies in the CR run overlap with that in Yajima et al. (2014a). However,  $f_{esc}$  of our simulations is somewhat lower in comparison. We have attributed this to differences in the SF recipes. The *Pressure* SF model (e.g., Dalla Vecchia & Schaye 2008; Schaye & Dalla Vecchia 2008; Choi & Nagamine 2010) have shown slower SFRs than the SF model based on the gas temperature and density used in Yajima et al. (2014a). The *Pressure* model allows the gas

to evolve to high-density,  $n_{\text{H}} > 100 \text{ cm}^{-3}$ , by delaying the SF. In the presence of high-density gas clumps, absorption of stellar radiation becomes more efficient, leading to somewhat lower  $f_{\text{esc}}$ . We note that at present, no preferred SF recipe in numerical simulations exist. One hopes that via comparison and constraining with observations, the correct physics of SF will be developed.

Massive galaxies with elevated SFR can be sources for the cosmic reionization. However, the mass dependence of  $f_{\text{esc}}$  for ionizing photons can suppress the ionizing photon emissivity of massive galaxies substantially (Yajima et al. 2011; Paardekoooper et al. 2013; Wise et al. 2014). In most cases, the escape fraction of the ionizing photons,  $f_{\text{esc}}^{\text{ion}}$ , will be smaller than that of the UV continuum photons (Yajima et al. 2014a). The former are also absorbed by hydrogen, whose optical depth can be much higher than that of dust. Therefore,  $f_{\text{esc}}^{\text{ion}}$  of massive galaxies can be much smaller than 0.1. Their rarity and small  $f_{\text{esc}}^{\text{ion}}$  make it doubtful that massive galaxies can serve as a major source of cosmic reionization.

The indicated upper limit of  $f_{\text{esc}}^{\text{ion}}$  for massive galaxies are smaller than that assumed in the observational studies (e.g., Ouchi et al. 2009; Bouwens et al. 2012). Wise et al. (2014) have shown recently that  $f_{\text{esc}}^{\text{ion}}$  decrease with the increasing stellar (galaxy) mass, and  $f_{\text{esc}}^{\text{ion}} < 0.1$  even for  $M_{\text{star}} \sim 10^6 M_{\odot}$  (see also, Yajima et al. 2011, 2014a). On the other hand, Kimm & Cen (2014) have shown that even galaxies with  $M_{\text{star}} \sim 10^6 - 10^8 M_{\odot}$  can have  $f_{\text{esc}}^{\text{ion}} \gtrsim 0.1$ . Although the values of  $f_{\text{esc}}^{\text{ion}}$  are being debated, most of the theoretical works agree that  $f_{\text{esc}}^{\text{ion}}$  decreases with increasing galactic stellar mass. Hence, massive galaxies like the observed bright LBGs and SMGs at  $z \gtrsim 6$  are not likely to have high  $f_{\text{esc}}^{\text{ion}}$ . Some observations have shown that  $f_{\text{esc}}^{\text{ion}} \gtrsim 0.1$  (e.g., Iwata et al. 2009; Cooke et al. 2014), while others point to  $f_{\text{esc}}^{\text{ion}} \lesssim 0.05$  (e.g., Siana et al. 2010; Vanzella et al. 2010). On the other hand, low-mass faint galaxies can have higher  $f_{\text{esc}}^{\text{ion}}$  (Yajima et al. 2011; Wise et al. 2014; Kimm & Cen 2014), and serve as the main ionizing sources, if the faint-end slope of the LF is steep ( $\alpha \lesssim -2$ , Bouwens et al. 2012; Jaacks et al. 2012). Future telescopes, such as the JWST or 30 m-class telescopes, will reveal the abundance of faint galaxies and allow to determine the ionizing sources in the high-redshift universe.

In summary, we have analysed the observational appearance of high-redshift galaxies evolving in rare overdense environment as well as in the average region of the universe, using the UV and IR bands and have reproduced their LFs. The average field galaxy LF (UCR run) has been compared with the observationally-deduced LFs and have been found in a very reasonable agreement. The overall impression is that these galaxies are compact, their SF sites appear to be heavily concentrated in the central regions, and are enshrouded in dust produced by the SN. The centrally-peaked dust distribution, therefore, results in substantial attenuating column densities and low escape fractions for the continuum UV photons, which decrease with the stellar mass in galaxies. We find that the redshift evolution of  $f_{\text{esc}}$  affects mostly the low-mass galaxies of  $M_{\text{star}} \lesssim 10^9 M_{\odot}$ , where  $f_{\text{esc}}$  increases by a factor of a few by  $z \sim 6$ . The emerging UV fluxes from massive galaxies in the overdense fields nevertheless can be detected by the current HST observations, but the detection depends on the galaxy aspect angle, if in-

deed there is a tendency for the more massive galaxies to be disk-like at these redshifts. Finally, we find that these massive galaxies above  $\sim 10^{9.5} M_{\text{star}}$  can be detected by ALMA below  $z \sim 10$  using reasonable integration time.

## ACKNOWLEDGMENTS

We thank Volker Springel for providing us with the original version of GADGET-3, and are grateful to Jun-Hwan Choi for valuable discussions. We thank the anonymous referee for useful comments. This work has been supported under the International Joint Research Promotion Program by Osaka University. I.S. has benefited from the partial support by the NSF and STScI. STScI is operated by AURA Inc., under NASA contract NAS 5-26555. E.R.D. thanks DFG for support under SFB 956. K.N. acknowledges the partial support by JSPS KAKENHI Grant Number 26247022.

## REFERENCES

- Biffi V., Maio U., 2013, MNRAS, 436, 1621  
 Bouwens R. J., Illingworth G. D., Franx M., Ford H., 2007, ApJ, 670, 928  
 Bouwens R. J. et al., 2009, ApJ, 705, 936  
 Bouwens R. J. et al., 2010, ApJ, 708, L69  
 Blanc G. A. et al., 2011, ApJ, 736, 31  
 Bouwens R. J. et al., 2011, ApJ, 737, 90  
 Bouwens R. J. et al., 2012, ApJ, 752, L5  
 Bouwens R. J. et al., 2014a, ApJ, 793, 115  
 Bouwens R. J. et al., 2014b, arXiv:1403.4295  
 Calzetti D., Armus L., Bohlin R. C., Kinney A. L., Koornneef J., Storchi-Bergmann T., 2000, ApJ, 533, 682  
 Cen R., Zheng Z., 2013, ApJ, 775, 112  
 Cen R., Kimm T., 2014, ApJ, 782, 32  
 Choi J.-H., Nagamine K., 2009, MNRAS, 393, 1595  
 —, 2010, MNRAS, 407, 1464  
 —, 2011, MNRAS, 410, 2579  
 Cooke J., Ryan-Weber E. V., Garel T., Díaz C. G., 2014, MNRAS, 441, 837  
 Dalla Vecchia C., Schaye J., 2008, MNRAS, 387, 1431  
 Dayal P., Ferrara A., 2012, MNRAS, 421, 2568  
 Dayal P., Dunlop J. S., Maio U., Ciardi B., 2013, MNRAS, 434, 1486  
 Di Matteo T., Springel V., Hernquist L., 2005, Nature, 433, 604  
 Draine B. T., 2003, ARA&A, 41, 241  
 Draine B. T., et al., 2007, ApJ, 663, 866  
 Dunkley J., et al., 2009, ApJ, 701, 1804  
 Dunlop J. S., McLure R. J., Robertson B. E., Ellis R. S., Stark D. P., Cirasuolo M., de Ravel L., 2012, MNRAS, 420, 901  
 Dunlop J. S. et al., 2013, MNRAS, 432, 3520  
 Eisenstein D. J., Hut P., 1998, ApJ, 498, 137  
 Ellis R. S. et al., 2013, ApJ, 763, L7  
 Fan X. et al., 2003, AJ, 125, 1649  
 Faucher-Giguère C.-A., Lidz A., Zaldarriaga M., Hernquist L., 2009, ApJ, 703, 1416  
 Finkelstein S. L. et al., 2013, Nature, 502, 524  
 Finkelstein S. L. et al., 2014, arXiv:1410.5439

- Finlator K., Oppenheimer B. D., Davé R., 2011, *MNRAS*, 410, 1703
- Gallerani S. et al., 2010, *A&A*, 523, 85
- Gronwall C. et al., 2007, *ApJ*, 667, 79
- Hatsukade B. et al., 2011, *MNRAS*, 411, 102
- Heller C. H., Shlosman I., Athanassoula E., 2007, *ApJ*, 671, 226
- Hirashita H., Ferrara A., Dayal P., Ouchi M., 2014, *MNRAS*, 443, 1704
- Hinschaw G. et al., 2013, *ApJS*, 208, 19
- Hoffman Y., Ribak E., 1991, *ApJ*, 380, L5
- Hopkins A. M., Beacom J. F., 2006, *ApJ*, 651, 142
- Inoue A. K., Buat V., Burgarella D., Panuzzo P., Takeuchi T. T., Iglesias-Páramo J., 2006, *MNRAS*, 370, 380
- Inoue A. K., Shimizu I., Tamura Y., Matsuo H., Okamoto T., Yoshida N., 2014, *ApJ*, 780, L18
- Iye M. et al., 2006, *Nature*, 443, 186
- Iwata I. et al., 2009, *ApJ*, 692, 1287
- Jaacks J., Choi J.-H., Nagamine K., Thompson R., Varghese S., 2012, *MNRAS*, 420, 1606
- Jaacks J., Thompson R., Nagamine K., 2013, *ApJ*, 766, 94
- Kennicutt Jr. R. C., 1998, *ARA&A*, 36, 189
- Kennicutt Jr. R. C., 1998, *ApJ*, 498, 541
- Kimm T., Cen R., 2013, *ApJ*, 776, 35
- Kimm T., Cen R., 2014, *ApJ*, 788, 121
- Leitherer C. et al., 1999, *ApJS*, 123, 3
- Li Y. et al., 2007, *ApJ*, 665, 187
- Li Y. et al., 2008, *ApJ*, 678, 41
- Madau P., Dickinson M., 2014, *ARA&A*, 52, 415
- Madau P., Haardt F., Rees M. J., 1999, *ApJ*, 514, 648
- Maiolino R. et al., 2008, *A&A*, 488, 463
- McLure R. J. et al., 2013, *MNRAS*, 432, 2696
- Meurer G. R., Heckman T. M., Calzetti D., 1999, *ApJ*, 521, 64
- Michałowski M. J., Dunlop J. S., Cirasuolo M., Hjorth J., Hayward C. C., Watson D., 2012, *A&A*, 541, A85
- Nakajima K., Ouchi M., Shimasaku K., Hashimoto T., Ono Y., Lee J. C., 2013, *ApJ*, 769, 3
- Nagamine K., Choi J.-H., Yajima H., 2010, *ApJ*, 725, 219
- Nagamine K., Ouchi M., Springel V., Hernquist L., 2010, *PASJ*, 62, 1455
- Nagamine K., Springel V., Hernquist L., Machacek M., 2004, *MNRAS*, 350, 385
- Nozawa T., Kozasa T., Habe A., 2006, *ApJ*, 648, 435
- Nozawa T., Kozasa T., Habe A., Dwek E., Umeda H., Tomonaga N., Maeda K., Nomoto K., 2007, *ApJ*, 666, 955
- Oesch P. A. et al., 2012, *ApJ*, 759, 135
- Oesch P. A. et al., 2013, *ApJ*, 773, 75
- Oesch P. A. et al., 2014, *ApJ*, 786, 108
- Ono Y. et al., 2012, *ApJ*, 744, 83
- Ono Y. et al., 2010, *MNRAS*, 402, 1580
- Ouchi M. et al., 2009, *ApJ*, 706, 1136
- Ouchi M. et al., 2004, *ApJ*, 611, 660
- Ouchi M. et al., 2004, *ApJ*, 611, 685
- Ouchi M. et al., 2010, *ApJ*, 723, 869
- Paardekooper J.-P., Khochfar S., Dalla Vecchia C., 2013, *MNRAS*, 429, L94
- Pawlik A. H., Milosavljević M., Bromm V., 2011, *ApJ*, 731, 54
- , 2013, *ApJ*, 767, 59
- Pettini M. et al., 2001, *ApJ*, 554, 981
- Riechers D. A. et al., 2013, *Nature*, 496, 329
- Romano-Díaz E., Shlosman I., Heller C., Hoffman Y., 2009, *ApJ*, 702, 1250
- Romano-Díaz E., Shlosman I., Trenti M., Hoffman Y., 2011a, *ApJ*, 736, 66
- Romano-Díaz E., Choi J.-H., Shlosman I., Trenti M., 2011b, *ApJ*, 738, L19
- Romano-Díaz E., Shlosman I., Choi J.-H., Sadoun R., 2014, *ApJ*, 790, L32
- Sadoun R., Shlosman I., Choi J.-H., Romano-Díaz E., 2015, in preparation
- Salpeter E. E., 1955, *ApJ*, 121, 161
- Schaerer D., 2003, *A&A*, 397, 527
- Schaerer D., de Barros S., 2009, *A&A*, 502, 423
- Schaye J., Dalla Vecchia C., 2008, *MNRAS*, 383, 1210
- Schneider R., Ferrara A., Salvaterra R., 2004, *MNRAS*, 351, 1379
- Shapley A. E., Steidel C. C., Pettini M., Adelberger K. L., 2003, *ApJ*, 588, 65
- Shibuya T., Kashikawa N., Ota K., Iye M., Ouchi M., Furusawa H., Shimasaku K., Hattori T., 2012, *ApJ*, 752, 114
- Shimizu I., Inoue A. K., Okamoto T., Yoshida N., 2014, *MNRAS*, 440, 731
- Shlosman I., 2013, in *Secular Evolution of Galaxies*, (eds.) J.Falcon-Barroso & J.H.Knapen, Cambridge, UK: Cambridge University Press, p.555
- Siana B. et al., 2010, *ApJ*, 723, 241
- Sijacki D., Springel V., Haehnelt, M.G., 2009, *MNRAS*, 400, 100
- Springel V., 2005, *MNRAS*, 364, 1105
- Springel V., Hernquist L., 2002, *MNRAS*, 333, 649
- , 2003a, *MNRAS*, 339, 289
- , 2003b, *MNRAS*, 339, 312
- Springel V. et al., 2005, *Nature*, 435, 629
- Springel V. et al., 2008, *MNRAS*, 391, 1685
- Stark D. P., Ellis R. S., Bunker A., Bundy K., Targett T., Benson A., Lacy M., 2009, *ApJ*, 697, 1493
- Stark D. P., Schenker M. A., Ellis R., Robertson B., McLure R., Dunlop J., 2013, *ApJ*, 763, 129
- Steidel C. C., Adelberger K. L., Giavalisco M., Dickinson M., Pettini M., 1999, *ApJ*, 519, 1
- Tanaka T. L., Li M., 2014, *ApJ*, 439, 1092
- Todini P., Ferrara A., 2001, *MNRAS*, 325, 726
- Tomassetti M., Porciani C., Romano-Díaz E., Ludlow A. D., Papadopoulos P. P., 2014, *MNRAS*, 445, L124
- van de Weygaert R., Bertschinger E., 1996, *MNRAS*, 281, 84
- Vanzella E. et al., 2010, *ApJ*, 725, 1011
- Vanzella E. et al., 2011, *ApJ*, 730, L35
- Verhamme A., Dubois Y., Blaizot J., Garel T., Bacon R., Devriendt J., Guiderdoni B., Slyz A., 2012, *A&A*, 546, A111
- Willott C. J., et al., 2010, *AJ*, 139, 906
- Wise J. H., Turk M. J., Norman M. L., Abel T., 2012, *ApJ*, 745, 50
- Wise J. H., Demchenko V. G., Halicek M. T., Norman M. L., Turk M. J., Abel T., Smith B. D., 2014, *MNRAS*, 442, 2560
- Yajima H., Choi J.-H., Nagamine K., 2011, *MNRAS*, 412, 411
- Yajima H., Li Y., Zhu Q., Abel T., 2012a, *MNRAS*, 424, 884
- Yajima H., Li Y., Zhu Q., Abel T., 2012b, submitted to



ApJ, arXiv:1211.0014  
Yajima H., Li Y., Zhu Q., Abel T., Gronwall C., Ciardullo R., 2012c, ApJ, 754, 118  
Yajima H., Choi J.-H., Nagamine K., 2012d, MNRAS, 427, 2889  
Yajima H., Li Y., Zhu Q., Abel T., Gronwall C., Ciardullo R., 2014a, MNRAS, 440, 776  
Yajima H., Nagamine K., Thompson R., Choi J.-H., 2014b, MNRAS, 439, 3073